KU LEUVEN

FACULTY OF SCIENCE

Solar cusp resonance

A study of the resonance of the slow surface mode in highly nonuniform solar cylinders

Pieter VANMECHELEN

Supervisor: Prof. T. Van Doorsselaere
KU Leuven

Thesis presented in
fulfillment of the requirements
for the degree of Master of Science
in Mathematics

Academic year 2019-2020

© Copyright by KU Leuven

Without written permission of the promotors and the authors it is forbidden to reproduce or adapt in any form or by any means any part of this publication. Requests for obtaining the right to reproduce or utilize parts of this publication should be addressed to KU Leuven, Faculteit Wetenschappen, Geel Huis, Kasteelpark Arenberg 11 bus 2100, 3001 Leuven (Heverlee), Telephone +32 16 32 14 01.

A written permission of the promotor is also required to use the methods, products, schematics and programs described in this work for industrial or commercial use, and for submitting this publication in scientific contests.

Preface

The overall aim of this thesis is to find general results for the slow resonance in solar cylinders of arbitrarily high degree of nonuniformity. Analytical calculations based on previous, similar work are provided. These are numerically implemented and some limitations regarding the considered method are pointed out. Finally, some possible additions to the model are proposed, but the implementation of these is left to future research.

Writing a thesis is no small task, and there are a number of people I would like to thank for helping me with this project. First and foremost, I want to thank my promotor, Tom Van Doorsselaere, for his expert guidance from start to finish. Without his help, this thesis would be nowhere near the quality it is now.

I would also like to give thanks to Jasper Wolfs, whose endless patience in discussing the Taylor series and their implementation is commendable. Similarly, thank you to Gregory Van Kruijsdijk for the many nightly discussions, which provided more insights than I'd dare to admit.

Another thank you I want to give to Eveline Wynendaele, who not only sat through the torment of proofreading this thesis on several occasions, but also provided me with countless tips regarding the form of a thesis.

Finally, I want to thank all my friends and family for their continued support throughout the process of writing this thesis.

List of symbols and abbreviations

MHD	Magnetohydrodynamics, 3
Mm	Megameter, 4
TT	Thin tube approximation, 8
TB	Thin boundary approximation, 9
TTTB	Thin tube and thin boundary approximation, 9

β	Plasma beta, 3
p_{th}	Thermal pressure, 4
p_{mag}	Magnetic pressure, 4, 5
$\mathbf{B}$	Magnetic field, 5
μ	Magnetic permeability of the vacuum, 5
ρ	Density, 5
v_S	Sound speed, 5
v_A	Alfvén speed, 5
v_C	Cusp speed, slow speed, 5
γ	Adiabatic index, 5
(r, φ, z)	Radial, azimuthal, longitudinal coordinates in a cylindrical coordinate system. When used as subscript these denote the corresponding component of a parameter, 6
t	Time, 6
m	Azimuthal wave number, 6
k_z	Longitudinal wave number, 6
ω	Frequency, 6
ω_S	Sound frequency, 7
ω_A	Alfvén frequency, 7
ω_C	Cusp frequency, slow frequency, 7
P	Total pressure, 5, 7
$\boldsymbol{v}$	Velocity, 7
$\boldsymbol{\xi}$	Lagrangian displacement, 7
R	Cylinder radius, 8
L	Cylinder length, 8
l	Thickness of the boundary layer in a cylindrical model, 8
I_m	Modified bessel function of the first kind of order m, 11
K_m	Modified bessel function of the second kind of order m, 11
r_c	Radial position of slow resonance, 12
ζ	Radial coordinate centered at the position of slow resonance, 12
$\mathcal{C}$	Coupling constant, 13, 17
ln	Natural logarithm, 13
$\mathbf{1}$	Indicator function, 14
$k_{\max}$	Truncation number of Taylor series, 22
θ_c	Relative position of slow resonance within the boundary layer, 35

Contents

Introduction

Magnetohydrodynamic waves occur throughout the solar atmosphere. These waves can broadly be classified in three groups: slow, fast and Alfvén waves. Classically, research has focused mostly on transverse waves, as these have been the easiest to observe. These transverse waves have a predominantly Alfvénic character, see e.g. Goossens et al. (2013). In recent years, the focus has broadened due to the detection of slow waves in magnetic pores in the lower atmosphere of the Sun (Dorotovič et al. 2008). Since then, the effect of the slow waves has been an increasingly relevant object of study.

In order to analytically study a structure such as a magnetic pore, it must be modelled in such a way that calculations can easily be done. The model used here is that of a magnetic cylinder. This is a widely used model (see e.g. Goossens et al. 1992) where the structure is modelled as a cylinder whose density, magnetic field strength and pressure vary from those of the background plasma. Typically, it is assumed that both the interior and the exterior regions are uniform. A nonuniform boundary layer can then be included such that the profiles of all parameters are continuous within the studied domain. A classical assumption is that this boundary layer is thin in comparison to the radius of the cylinder. However, it has been shown by Van Doorsselaere et al. (2004) and later by Soler et al. (2014) that the expressions obtained from this assumption lead to significant errors when compared to fully numerical calculations. Hence in this thesis the assumption of a thin boundary layer will be discarded and the boundary layer can have an arbitrary thickness, which allows for the study of highly nonuniform cylinders.

The slow waves have a characteristic frequency which depends on the plasma density, pressure and magnetic field strength. By considering a cylinder with a boundary layer, these parameters and thus also this slow frequency have a continuous variation within the boundary layer, changing from a uniform internal to a uniform external value. Similarly, every wave mode of the magnetic pore has a specific frequency. For slow surface wave modes, this frequency lies between the internal and external slow frequencies, as shown by e.g. Edwin & Roberts (1983). Hence, because the profile is continuous, there is a point where the slow frequency is equal to the frequency of the surface mode. As a result, a resonance will occur at this point. This resonance causes a loss of energy from the global surface mode to localised modes, resulting in resonant damping of the surface mode (see e.g. Edwin & Roberts 1983).

Understanding the damping of the slow waves is a crucial part of the study of these waves. Observations suggest that this damping is quite strong, see e.g. Krishna Prasad et al. (2014), Grant et al. (2015). Several other mechanisms have been suggested to explain this strong damping. For example, Mandal et al. (2016) propose a damping by thermal conduction. In this thesis, only the effect of resonant absorption is considered. Regarding this resonant damping, it was previously believed that the damping due to the

slow resonance is much weaker than damping due to Alfvén resonance (see e.g. Soler et al. 2009), however Yu et al. (2017a) show that under magnetic pore conditions this is not the case.

The equations that govern a system such as a magnetic pore have been known for several decades (see e.g Goossens et al. 1992). Within the uniform layers they can easily be solved, but in the boundary layer this calculation is more involved. The method used here will be based on the method used by Soler et al. (2013) who studied the Alfvén resonance in the solar corona. This method consists of constructing a Frobenius expansion at the point of resonance, such that an approximation to the true solution can be found within the boundary layer. For comparison, the results obtained with this method will then be studied in the limiting case of a thin boundary. For the limit of a thin boundary, results have already been obtained by Yu et al. (2017a), who studied the slow resonance specifically in this thin boundary limit.

When the dispersion relation is known, it can be implemented to study the slow resonance. Because the dispersion relation is derived from eigenfunctions which are constructed as Frobenius expansions, this must happen numerically, as shown by Soler et al. (2013). For a numerical implementation it is then necessary to specify the profiles of all parameters in order to construct these eigenfunctions. The implementation of these profiles is not straightforward. The profiles must be implemented as Taylor series and they must be consistent with each other. As it turns out, the behaviour of this Taylor series cannot be controlled for simple profiles and they will not always be convergent. As a result, the solution to the dispersion relation is not found numerically, but several possible solutions to this divergence problem are proposed.

This Master's thesis is presented in three chapters. In the first chapter, the general configuration of the system is explained, as well as the governing equations. The second chapter then covers the analytic calculation of the dispersion relation and relates this to previous results. Finally, the third chapter is concerned with the numerical implementation of the analytical results. In this third chapter the methodology is first explained and then attention is given to the divergent behaviour which limits the method. Finally, three proposed alternative methods are given which may yield solutions, but none of them are implemented and a rigorous study of these is left to future research.

Chapter 1

Configuration of a magnetic cylinder

1.1 Equilibrium configuration

The solar atmosphere is a very complex system consisting of three main layers. The first layer, which can be viewed as the surface of the sun, is the photosphere. It is a relatively cool and dense region, with a temperature on the order of 6,000 Kelvin. The next layer is the chromosphere, which is a region where density gradually decreases leading to the outermost layer, the solar corona. The corona, depending on the degree of activity, may extend up to three solar radii. It is a very tenuous region, with a density many orders of magnitude lower than the photosphere. Despite this, the corona is extremely hot, having a temperature exceeding one million Kelvin. The cause of this high temperature remains unknown: this problem is known as the coronal heating problem and is the topic of intense study (Aschwanden 2005).

Since the second half of the 20th century and the advent of space-based telescopes, the quality of observations of the solar atmosphere has improved immensely. This improvement has been continuing into the 21st century with recent missions such as the Parker Solar Probe, which launched in 2018. This progress has enabled observational research to an unprecedented degree. On the theoretical side, progress has been equally remarkable. The solar atmosphere is a plasma, which is a magnetized fluid. In order to study plasmas, a framework is needed that can incorporate both the thermal effects from the fluid aspect of the plasma and the magnetic effects. Such a framework is provided by magnetohydrodynamics, or MHD for short. The field of MHD was pioneered by Hannes Alfvén in the middle of the 20th century. In 1970, Alfvén was awarded the Nobel Prize in Physics for this contribution (Nakariakov et al. 2016).

Depending on the structure of the plasma, the thermal and magnetic effects can be comparable in strength, or one can be stronger than the other. For example, in a plasma which is only slightly magnetised, the thermal effects outweigh the magnetic, and the plasma behaves largely as an unmagnetized fluid. A dimensionless parameter which is often used to quantify the relative difference between the two effects is the plasma beta β. It is simply defined as the ratio between the thermal and magnetic pressure of the plasma:

$$\beta = \frac{p_{\mathrm{th}}}{p_{\mathrm{mag}}}. \tag{1.1}$$

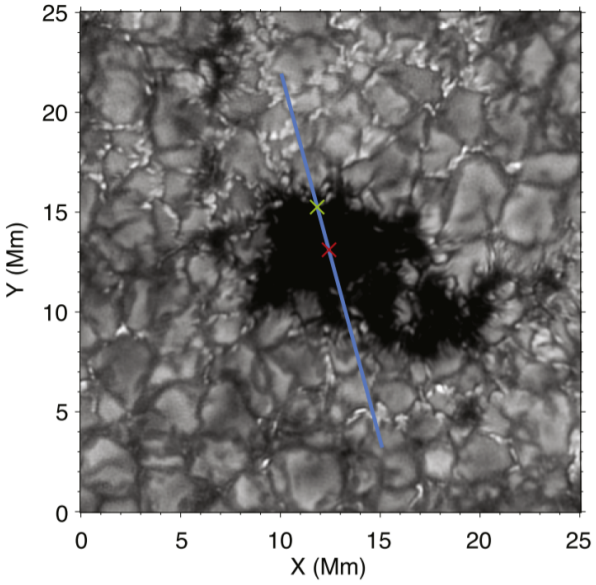

Figure 1.1: Detail of a magnetic pore in the photosphere. The pore size is approximately 10 Mm, which is on the order of 0.01% of the surface area of the photosphere. Figure taken from Keys et al. (2018).

The value of β gives an immediate qualitative impression of the structure of the plasma. If $\beta \ll 1$, the plasma is dominated by magnetic effects and vice versa if $\beta \gg 1$. The thermal and magnetic pressures are not only relevant for classifying different plasmas, but also play an important role in the study of solar atmospheric structures. Due to the complicated physics in the atmosphere of the Sun, many structured regions may appear where the plasma parameters differ from the surrounding, "quiet" Sun. These structures range from coronal loops, which are long, thin loops that extend deep into the corona, to massive coronal holes at the north and south poles which are large regions dominated by open magnetic field lines (Aschwanden, 2005). One structure which will be the main focus of this study is the magnetic pore, as seen in figure 1.1. This is a fairly small-scale photospheric structure, on the order of a few Mm in size (Grant et al. 2015, Keys et al. 2018). It is characterized as a region where the magnetic field is several orders of magnitude greater than in the surrounding photosphere (Aschwanden, 2005). This has the interesting effect that inside the pore, the plasma is dominated by magnetic effects and thus $\beta < 1$, while outside the thermal effects are more important and here $\beta > 1$.

In order to study structures such as magnetic pores, a simple way of modelling them is required. Perhaps the easiest model, which has been used in the past (see e.g. Edwin & Roberts, 1982), is the slab geometry. This models the structure in one dimension with a simple step function profile. A slightly more accurate version of this is a simple cylinder. By assuming cylindrical symmetry, this is still a one-dimensional profile, where the only variation is in the radial direction. The cylindrical model is an effective tool which is still in wide use today (see e.g. Soler et al. 2013, Yu et al. 2017a).

The atmospheric structures typically have lifetimes on the order of hours to days, hence they tend to be quite stable. This means that in equilibrium the total pressure, which is the sum of the thermal and magnetic pressures, is constant over both the in- and outside of the structure. If this were not the case, the pressure imbalance would cause the structure to dissipate and there would not be an equilibrium. In the case of a one-dimensional

cylindrical model, the condition of constant pressure is simply

$$\frac{d}{dr}\Big(p_{\mathrm{th}} + p_{\mathrm{mag}}\Big) = 0. \tag{1.2}$$

In order to perform calculations with the total pressure, an expression for the magnetic pressure is needed. To this end, the magnetic field is written as $\mathbf{B}$. Then the magnetic pressure is expressed as

$$p_{\mathrm{mag}} = \frac{B^2}{2\mu}. \tag{1.3}$$

Here B^2 is defined as $\mathbf{B}\cdot\mathbf{B}$ and μ is the permeability of the vacuum, which in SI units has a value of $4\pi \cdot 10^{-7}$ H/m. In the cylindrical model, it is often assumed that the magnetic field is straight and aligned with the cylinder axis. The coordinate system is constructed with the z-axis along the axis of the cylinder. In the one-dimensional case of cylindrical symmetry, the magnetic field at equilibrium can then be written as $\mathbf{B} = (0, 0, B(r))$. Together with the magnetic field and the thermal pressure, another parameter of interest is the plasma density ρ. From these three parameters, three characteristic plasma speeds can be defined. These are the sound, Alfvén and cusp speeds. Following Goossens et al. (1992), their squares are defined as

$$v_S^2 = \frac{\gamma p_{\mathrm{th}}}{\rho}, \qquad v_A^2 = \frac{B^2}{\mu\rho}, \qquad v_C^2 = \frac{v_S^2 v_A^2}{v_S^2 + v_A^2}, \tag{1.4}$$

respectively. γ in the expression of the sound speed is the adiabatic index. For a hydrogen plasma, which is a good approximation for the solar atmosphere, γ has a value of 5/3. It is further assumed that the plasma is ideal, meaning that the effects of viscosity are neglected. The sound speed for plasmas is the same as for fluids, where it is the only nonzero of the three due to the absence of a magnetic field. It arises solely from thermal effects. The Alfvén speed, named after Hannes Alfvén, can be seen as the magnetic equivalent to the sound speed. From these two speeds, the cusp speed can be defined. It is immediately clear from this definition that the cusp speed is always smaller than the other two, which explains its other name: the slow speed. The cusp speed is most relevant in plasmas where $\beta \approx 1$: if β is much larger or smaller than 1, then one of the slow and Alfvén speeds will be much larger than the other and of course also much larger than the slow speed. The two slower speeds, of which the cusp speed is then always one, will be negligible compared to the faster speed. Hence in these limits, only one of the characteristic speeds is relevant and the cusp speed will always be negligible compared to this more relevant speed. For example, in the solar corona the plasma β is on the order of 10^{-2} and here a common assumption is $v_S = v_C = 0$, since both are much smaller than the Alfvén speed in this case. Hence only the Alfvén speed is typically studied in the corona. For magnetic pores, the cusp speed is relevant because the plasma β is smaller than 1 in the interior of the pore, and larger than 1 in the exterior. Within the transitional region β will then cross 1, which explains the specific interest in this particular structure.

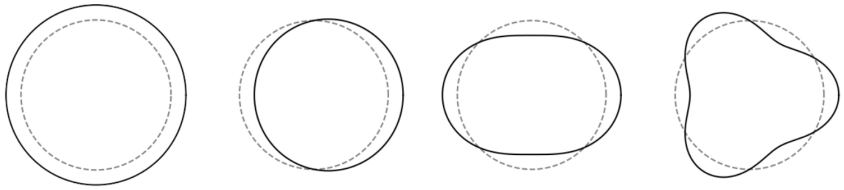

Figure 1.2: Different azimuthal wave modes for integer values of m. From left to right: the sausage mode $m = 0$, the kink mode $m = 1$ and fluting modes for $m = 2, 3$. The cylinder at equilibrium is drawn in dashed lines, perturbations are drawn in solid lines.

1.2 Perturbed quantities

The quantities introduced so far are used to describe a stationary equilibrium. To study the behaviour of MHD waves, a perturbation is imposed on the equilibrium. It is assumed that this perturbation is small, such that its effects can be linearised and the higher-order effects can be neglected. A cylindrical model for the pore is considered, as done by e.g. Yu et al (2017a). Hence the pore can be seen as a flux tube. The coordinate system is written as (r, φ, z), and time is denoted as t. Because in this one-dimensional model the equilibrium values are assumed to only depend on the radial coordinate r, the perturbed quantities can be Fourier-analysed with respect to the other coordinates φ, z and t. A detailed explanation of this method is given by Goossens et al. (1992). In this analysis, every quantity f can be written as

$$f = f'(r) \exp\big(i(m\varphi + k_z z - \omega t)\big). \tag{1.5}$$

Here ω is the frequency, m is the azimuthal wave number and k_z the longitudinal wave number. Typically only integer values of m are considered, since these give rise to standing waves, as shown in figure 1.2. The different azimuthal wave modes have distinct behaviour. When $m = 0$, the resulting behaviour is an alternating compression and rarefaction of the plasma inside the cylinder. This is called the sausage mode. For a value of $m = 1$, the wave mode is a transverse displacement of the loop axis, which is known as the kink mode. If $m \geq 2$, the wave mode is characterised as a deformation of the shape of the cylinder. These higher-order modes are called fluting modes and they are typically considered to be less important, since they have not yet been identified in solar observations (Nakariakov et al. 2016).

The longitudinal wave number k_z also takes on a value that results in standing waves, this time in the z-direction. Hence the ends of the cylinder are stationary under this condition. Quantitatively, this means that k_z is assumed to be an integer multiple of π/L, where L is the length of the tube. When $k_z = \pi/L$, there is only one wave top in the longitudinal direction. This is called the fundamental mode and is typically the most studied mode. Furthermore, the longitudinal wave number is used to define different plasma frequencies from the three characteristic speeds. These frequencies are aptly named the sound, Alfvén and cusp frequency, corresponding to the respective speed. They are denoted as ω_S, ω_A and ω_C, respectively. In a region where the oscillation frequency ω is equal to one of the plasma frequencies, a resonance will occur which will cause an absorption of energy and a subsequent damping of the oscillation. The focus here will be on the cusp resonance, which occurs when the frequency is equal to the cusp frequency. The frequencies are

defined through the characteristic speeds as

$$\omega_S = k_z v_S, \qquad \omega_A = k_z v_A, \qquad \omega_C = k_z v_C. \tag{1.6}$$

The Fourier analysis gives a straightforward treatment of the azimuthal, longitudinal and time component. The radial component is more involved. Following Goossens et al. (1992), the calculations for this component start with the total pressure. With the previously introduced definitions of total and magnetic pressure, the radial component of the perturbed total pressure, P', can be written as

$$P' = p'_{\text{th}} + \frac{\mathbf{B} \cdot \mathbf{B}'}{\mu}, \tag{1.7}$$

where p'_{th} and $\mathbf{B}'$ are the perturbed thermal pressure and magnetic field, respectively. Another quantity which is used in the calculations is the radial velocity v'_r. However, as shown by Goossens et al. (1992), it turns out that the calculations can be made much simpler by instead working with the radial component of the Lagrangian displacement $\boldsymbol{\xi}$ instead of $\boldsymbol{v}'$. These two equations are simply related as

$$\boldsymbol{v}' = \frac{d\boldsymbol{\xi}}{dt}. \tag{1.8}$$

The current focus lies mostly on the radial component of $\boldsymbol{\xi}$, which will be denoted as ξ_r. It has been shown by Goossens et al. (1992) that the perturbed total pressure and Lagrangian displacement can be related through the following system of equations:

$$D\frac{d}{dr}(r\xi_r) = -C_1 r P', \tag{1.9a}$$

$$D\frac{dP'}{dr} = C_2 \xi_r, \tag{1.9b}$$

where

$$D = \rho(v_S^2 + v_A^2)(\omega^2 - \omega_A^2)(\omega^2 - \omega_C^2), \tag{1.10a}$$

$$C_1 = \omega^4 - (v_S^2 + v_A^2)\left(\frac{m^2}{r^2} + k_z^2\right)(\omega^2 - \omega_C^2), \tag{1.10b}$$

$$C_2 = \rho^2(v_S^2 + v_A^2)(\omega^2 - \omega_A^2)^2(\omega^2 - \omega_C^2). \tag{1.10c}$$

The expressions of D and $C_{1,2}$ depend on the radial coordinate r through the density and characteristic speeds. The system of equations 1.9 will be solved in the next section to yield expressions for P' and ξ_r.

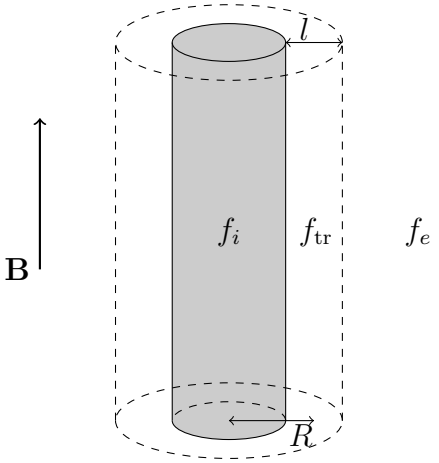

Figure 1.3: The general set-up of the cylinder. The subscript i is used for parameters inside the cylinder, subscript e for outside. These subscripts will be used together with the subscripts denoting sound, Alfvén or cusp parameters as well. Both regions are connected by a nonuniform boundary layer.

1.3 Cylinder configuration

In order to solve the equations for the total pressure and Lagrangian displacement, some closer attention should be paid to the configuration of the system. As mentioned before, the pore is modelled as a cylinder. It is assumed that the background magnetic field is straight and uniform both in the interior and exterior of the tube. The cylinder can then be aligned with this magnetic field. Then the cylindrical coordinate system can have its z-axis aligned with these as well, ensuring that the magnetic field has only a component in the z-direction, as mentioned before. Next, if the radius of the cylinder is written as R, it is assumed that $k_z R \ll 1$. This is the so-called thin tube (TT) approximation, since it is essentially equivalent to $R \ll L$. The TT approximation is often adopted, see e.g. Van Doorsselaere et al. 2004.

In the one-dimensional model, all parameters are assumed to only have a radial dependence. The simplest form of this dependence would be a step profile, where there is a constant interior and a constant exterior value with a discontinuous jump in between. This is not a very realistic profile, however, since the edges of solar atmospheric structures are typically not sharply defined. A better model then includes a transitional layer where all parameters change continuously from their internal to their external values. Of course, within this transitional boundary layer the parameters are not uniform and a profile for this variation should be specified. Later in this Master's thesis, two profiles for the boundary layer are considered: a linear and sinusoidal profile. For now, the specific shape of this profile is left unspecified. Following Soler et al. (2013) and by denoting the thickness of the boundary layer as l, any parameter f can then be written as

$$f(r) = \begin{cases} f_i & \text{if } r \leq R - l/2, \\ f_{\rm tr}(r) & \text{if } R - l/2 < r < R + l/2, \\ f_e & \text{if } r \geq R + l/2. \end{cases} \tag{1.11}$$

This general set-up is sketched in figure 1.3. An important quantity here is the thickness of the boundary layer, l. A thickness of $l = 0$ corresponds to the simple step profile,

while a thickness of $l = 2R$ would correspond to a fully inhomogeneous cylinder. A classical assumption which is often made, is $l \ll R$. This is the so-called thin boundary (TB) assumption. The combination of the thin boundary assumption with the thin tube assumption is called the thin tube and thin boundary (TTTB) assumption.

In the TTTB approach, the system of equations 1.9 is solved in the uniform interior and exterior layers. Treatment of this system in the nonuniform layer is avoided by imposing jump conditions across the boundary layer. A more detailed explanation of this approach can be found in Goossens et al. (1992). The TTTB method allows for analytical expressions to be found for the frequency and damping rate of the oscillations. Although the TTTB assumption is often adopted (see e.g. Goossens et al. 1992, Yu et al. 2017a), it has been shown that this assumption becomes invalid for larger values of l/R. Van Doorsselaere et al. (2004) compared the analytical results obtained from the TTTB formula to numerical calculations for arbitrary values of l/R. They found that for highly nonuniform solar flux tubes the TTTB formula underestimates the damping rate. In the case of a fully nonuniform tube ($l/R = 2$), they found that the damping rate is underestimated by about 25% when compared to numerical results. In their paper, a sinusoidal profile of the density in the boundary layer was considered. Soler et al. (2014) subsequently calculated the error of the TTTB approximation for a linear and parabolic profile. They found that for these profiles the understimation of the damping rate in the TTTB approximation was even greater. In the case of a fully nonuniform tube, an error exceeding 50% was found.

In the more general approach of arbitrary boundary layer thickness, the system of equations is solved not only in the uniform regions, but also in the boundary layer. In this region, all parameters have a non-constant radial dependence, which can take many different forms. Keeping this in mind, equations 1.9 can be combined into one second-order ordinary differential equation for P', which is

$$\frac{d^2P'}{dr^2} + \frac{d/dr\,(Dr/C_2)}{Dr/C_2}\frac{dP'}{dr} + \frac{C_1C_2}{D^2}P' = 0. \tag{1.12}$$

Substituting the expressions from equations 1.10, this equation can be rewritten as

$$\frac{d^2P'}{dr^2} + \left(\frac{1}{r} - \frac{d/dr(\rho(\omega^2-\omega_A^2))}{\rho(\omega^2-\omega_A^2)}\right)\frac{dP'}{dr} + \left(\frac{(\omega^2-\omega_S^2)(\omega^2-\omega_A^2)}{(v_S^2+v_A^2)(\omega^2-\omega_C^2)} - \frac{m^2}{r^2}\right)P' = 0. \tag{1.13}$$

This is the general equation that will be solved in the following chapter. In the uniform regions, the plasma parameters are constant and this equation reduces to

$$\frac{d^2P'}{dr^2} + \frac{1}{r}\frac{dP'}{dr} + \left(\frac{(\omega^2-\omega_S^2)(\omega^2-\omega_A^2)}{(v_S^2+v_A^2)(\omega^2-\omega_C^2)} - \frac{m^2}{r^2}\right)P' = 0, \tag{1.14}$$

which is the classical equation discussed by Goossens et al. (1992) in a uniform plasma. A different limit of equation 1.13 is when $\beta \to 0$. In this limit, the equation reduces to

$$\frac{d^2P'}{dr^2} + \left(\frac{1}{r} - \frac{d/dr(\rho(\omega^2-\omega_A^2))}{\rho(\omega^2-\omega_A^2)}\right)\frac{dP'}{dr} + \left(\frac{\omega^2-\omega_A^2}{v_A^2} - \frac{m^2}{r^2}\right)P' = 0. \tag{1.15}$$

This is the equation studied by Soler et al. (2013), who researched the Alfvén resonance in the limit of $\beta = 0$. In any case, from the solution for P' an expression for ξ_r can be found as

$$\xi_r = \frac{1}{\rho(\omega^2 - \omega_A^2)} \frac{dP'}{dr}. \tag{1.16}$$

In the following chapter, equation 1.13 will be studied to derive the dispersion relation for the slow surface waves.

Chapter 2

Analytic calculations

2.1 Solutions in a uniform region

Resonance occurs at a point where the frequency of a wave mode is equal to a characteristic frequency at that point. In the case of the cusp resonance, this means that there is a point where $\omega = \omega_C$. The interval between the internal and external cusp frequencies is called the slow continuum. Because the cusp frequency varies continuously from its internal to its external value in the transitional layer, it takes on every intermediary value within this layer. Hence, if there is a wave mode which has a frequency between ω_{Ci} and ω_{Ce}, there will be a point at which this frequency is equal to the cusp frequency and cusp resonance will occur at this position. An important quantity in characterising different modes is

$$k_\perp^2 = -\frac{(\omega^2 - \omega_S^2)(\omega^2 - \omega_A^2)}{(v_S^2 + v_A^2)(\omega^2 - \omega_C^2)}, \tag{2.1}$$

which occurs in equation 1.13. For body waves, this quantity is negative. In the case of surface waves, $k_\perp^2$ is positive, as explained by Edwin & Roberts (1983). This explains the minus sign in equation 2.1: it guarantees that $k_\perp^2$ is positive for the surface mode, such that $k_\perp$ is a real quantity, which will be useful for the upcoming calculations. In figure 2.1 phase speed diagrams are plotted for several of these modes. Here it is clear that the slow surface mode is of special interest: for this mode the phase speed lies between the internal and external cusp speeds. It should be noted that in this particular case the external cusp speed is zero. Because of this, there will be a position where slow resonance occurs for the slow surface mode. Hence this mode will be focused on from now on.

Equation 1.13 can be straightforwardly solved in the internal and external regions. Here all parameters are uniform, so the equation reduces to

$$\frac{d^2P'}{dr^2} + \frac{1}{r}\frac{dP'}{dr} + \left(\frac{(\omega^2 - \omega_S^2)(\omega^2 - \omega_A^2)}{(v_S^2 + v_A^2)(\omega^2 - \omega_C^2)} - \frac{m^2}{r^2}\right) P' = 0. \tag{2.2}$$

This is Bessel's equation. To determine which Bessel function solves this equation, a boundary condition is needed. For the interior region, the additional requirement is that P' is regular at $r = 0$. Because the surface modes are considered, this then means that the solution is

$$P_i' = A_i I_m(k_{\perp,i} r), \tag{2.3}$$

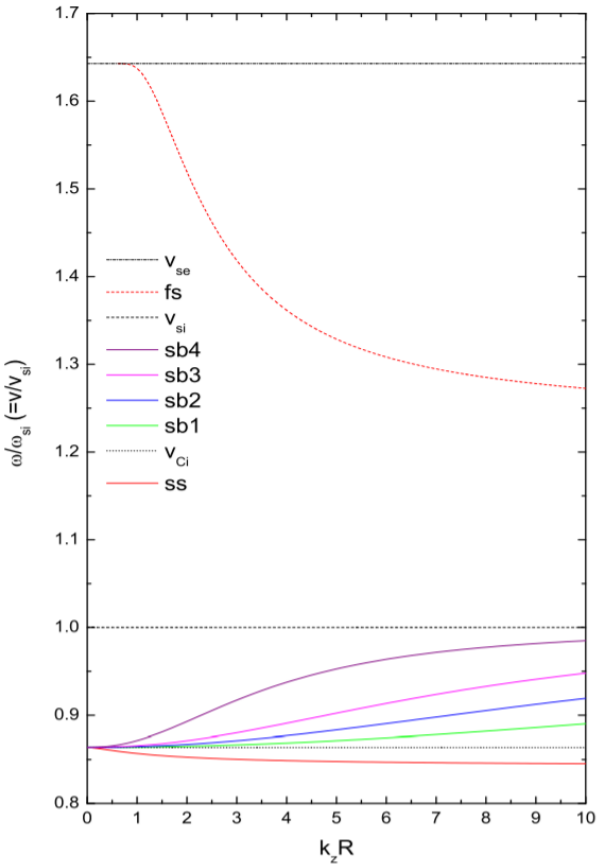

Figure 2.1: Phase speeds ω/ω_{Si} as a function of $k_z R$ for a fast surface (fs), slow surface (ss) and several slow body (sb) modes. All modes are sausage modes ($m = 0$). Phase speeds are normalised with respect to internal sound speed and measured under magnetic pore conditions. Under these conditions, $v_{Ce} = 0$. Figure taken from Yu et al. (2017a).

as shown by Goossens et al. (1992). Here I_m is the modified Bessel function of the first kind of order m, A_i is an integration constant and

$$k_{\perp,i}^2 = -\frac{(\omega^2 - \omega_{Si}^2)(\omega^2 - \omega_{Ai}^2)}{(v_{Si}^2 + v_{Ai}^2)(\omega^2 - \omega_{Ci}^2)}. \tag{2.4}$$

Solving equation 2.2 in the exterior region is straightforward as well. This time, the condition holds that the perturbation must disappear as $r \to \infty$. Again following Goossens et al. (1992), the solution in the exterior layer is

$$P_e' = A_e K_m(k_{\perp,e} r), \tag{2.5}$$

where K_m is the modified Bessel function of the second kind of order m, A_e is a constant and

$$k_{\perp,e}^2 = -\frac{(\omega^2 - \omega_{Se}^2)(\omega^2 - \omega_{Ae}^2)}{(v_{Se}^2 + v_{Ae}^2)(\omega^2 - \omega_{Ce}^2)}. \tag{2.6}$$

With the expressions for P' know, expressions for ξ_r can be found from equation 1.16. For the interior and exterior layers, these are

$$\xi_{ri} = \frac{A_i k_{\perp,i}}{\rho_i(\omega^2 - \omega_{Ai}^2)} I'_m(k_{\perp,i} r), \tag{2.7a}$$

$$\xi_{re} = \frac{A_e k_{\perp,e}}{\rho_e(\omega^2 - \omega_{Ae}^2)} K'_m(k_{\perp,e} r). \tag{2.7b}$$

Here the prime at the Bessel functions denotes their derivative with respect to the argument. These expressions will later be coupled to the solution in the boundary layer to obtain the dispersion relation.

2.2 Solutions in a nonuniform region

Solving equation 1.13 in the boundary layer is more involved than in the uniform regions. Because now the plasma parameters are no longer constant, the equation needs to be treated in full. To this end, a change in coordinate is performed. This is similar to the method used by Soler et al. (2013) for the Alfvén resonance. If the position of the cusp resonance within the boundary layer is denoted as $r = r_c$, this new coordinate can be defined as

$$\zeta = r - r_c, \tag{2.8}$$

such that the resonant position is situated at $\zeta = 0$. In this coordinate, the inner and outer edges of the boundary layer can be defined as

$$\zeta_i = R - \frac{l}{2} - r_c, \tag{2.9a}$$

$$\zeta_e = R + \frac{l}{2} - r_c, \tag{2.9b}$$

respectively. It is straightforward to rewrite equation 1.13 in terms of ζ:

$$\begin{aligned} &\frac{d^2 P'}{d\zeta^2} + \left(\frac{1}{\zeta + r_c} - \frac{d/d\zeta(\rho(\omega^2 - \omega_A^2))}{\rho(\omega^2 - \omega_A^2)} \right) \frac{dP'}{d\zeta} \\ &+ \left(\frac{(\omega^2 - \omega_S^2)(\omega^2 - \omega_A^2)}{(v_S^2 + v_A^2)(\omega^2 - \omega_C^2)} - \frac{m^2}{(\zeta + r_c)^2} \right) P' = 0. \end{aligned} \tag{2.10}$$

In order to keep the upcoming calculations reasonably compact, a shorthand notation is introduced to rewrite this equation. In this notation, equation 2.10 can be rewritten as

$$\zeta^2 h(\zeta) \frac{d^2 P'}{d\zeta^2} + \zeta p(\zeta) \frac{dP'}{d\zeta} + q(\zeta) P' = 0, \tag{2.11}$$

where

$$f(\zeta) = \rho(\omega^2 - \omega_A^2), \tag{2.12a}$$
$$h(\zeta) = (\zeta + r_c)^2 f(\zeta), \tag{2.12b}$$
$$p(\zeta) = \zeta(\zeta + r_c)\left(f(\zeta) - (\zeta + r_c)\frac{df(\zeta)}{d\zeta}\right), \tag{2.12c}$$
$$q(\zeta) = \zeta^2\left((\zeta + r_c)^2 f(\zeta)\frac{(\omega^2 - \omega_S^2)(\omega^2 - \omega_A^2)}{(v_S^2 + v_A^2)(\omega^2 - \omega_c^2)} - m^2 f(\zeta)\right). \tag{2.12d}$$

To find the solution for P' of equation 2.11, the same method is used as Soler et al. (2013) did for the Alfvén resonance. The perturbed total pressure is expressed as a Frobenius series around the resonance position $\zeta = 0$:

$$P'_{\text{tr}} = \sum_{k=0}^{\infty} p'_k \zeta^{k+s}. \tag{2.13}$$

The coefficients p'_k in this expression depend on the profiles chosen for the characteristic speeds and plasma parameters in the transitional layer. s is the index of the expansion. To find the value of s, equation 2.13 is substituted in equation 2.11. In the resulting equation, the coefficients of lowest order of ζ determine the so-called indicial equation, which defines the value of s. In this case, Goossens et al. (1992) show that the indicial equation is $s(s-1) = 0$. Knowing this indicial equation, the solution for P'_{tr} can be written as

$$P'_{\text{tr}}(\zeta) = A_0 P'_1(\zeta) + S_0 P'_2(\zeta), \tag{2.14}$$

where

$$P'_1(\zeta) = \sum_{k=0}^{\infty} \alpha_k \zeta^{k+1}, \tag{2.15a}$$
$$P'_2(\zeta) = \sum_{k=0}^{\infty} \sigma_k \zeta^k + \mathcal{C} P'_1(\zeta)\ln(\zeta). \tag{2.15b}$$

Because there is an integer difference between the two roots of the indicial equation, a logarithmic term arises in the expression of P'_2. $\mathcal{C}$ is a constant, which is called the coupling constant. The other constants A_0 and S_0 are arbitrary: P'_1 and P'_2 are linearly independent solutions of equation 2.11, so any linear combination of them yields a solution as well. In the following calculations, both P'_1 and P'_2 will occasionally be studied independently. To this end, P'_1 is called the regular solution and it can in general be studied by taking $A_0 = 1, S_0 = 0$ in the general expression for P'_{tr}. Similarly, P'_2 will be called the singular solution and can be found by taking $A_0 = 0, S_0 = 1$ in P'_{tr}. The coefficients α_k and σ_k can then be determined by substituting the expressions for P'_1 and P'_2 into equation 2.11. In order to do this, not only is a general expression for P'_{tr} needed, but also for its first

and second order derivatives with respect to ζ. Substituting equations 2.15 into equation 2.14, the expressions are

$$P'_{\text{tr}} = \sum_{k=0}^{\infty} \Big[(A_0 + S_0\mathcal{C}\ln(\zeta))\alpha_{k-1}\mathbf{1}_{k\geq 1} + S_0\sigma_k \Big]\zeta^k, \tag{2.16a}$$

$$\frac{\partial P'_{\text{tr}}}{\partial \zeta} = \sum_{k=0}^{\infty} \Big[\Big((k+1)(A_0 + S_0\mathcal{C}\ln(\zeta)) + S_0\mathcal{C} \Big)\alpha_k + (k+1)S_0\sigma_{k+1} \Big]\zeta^k, \tag{2.16b}$$

$$\begin{aligned}\frac{\partial^2 P'_{\text{tr}}}{\partial \zeta^2} = \sum_{k=-1}^{\infty} \Big[&\Big((k+1)(k+2)(A_0 + S_0\mathcal{C}\ln(\zeta)) + (2k+3)S_0\mathcal{C} \Big)\alpha_{k+1} \\ &+ (k+1)(k+2)S_0\sigma_{k+2} \Big]\zeta^k.\end{aligned} \tag{2.16c}$$

In these expressions $\mathbf{1}_{\mathcal{P}}$ is the indicator function, which is 1 if $\mathcal{P}$ holds and 0 elsewhere. This indicator function is introduced to allow for the notation of all three quantities as power series in ζ, which will be useful for ease of future calculations. An interesting result here is that the second derivative of P'_{tr} contains a term in ζ^{-1}. This is a consequence of the $\zeta\ln(\zeta)$-term that arises in the singular solution. This already points to a difference with the case of Alfvén resonance. As shown by Goossens et al. (1992), in the case of Alfvén resonance the indicial equation is $s(s-2) = 0$. Hence there is no $\zeta\ln(\zeta)$-term in this case and the second derivative of P'_{tr} will not contain a pole-order term.

The goal is now to write equation 2.11 in its entirety as a power series in ζ. For this power series expressions of f, h, p and q are needed. To this end, it is assumed that the profiles of cusp, sound and Alfvén speeds, as well as those of density and magnetic field can be expanded themselves as Taylor series within the boundary layer. For the density and magnetic field, these expansions will be denoted as

$$\rho(\zeta) = \sum_{k=0}^{\infty} \rho_k \zeta^k, \tag{2.17a}$$

$$\mathbf{B}^2(\zeta) = \sum_{k=0}^{\infty} B_k^2 \zeta^k. \tag{2.17b}$$

With these expressions, expansions for f, h and p can be readily obtained. The expansion coefficients of f will be used throughout the upcoming calculations, as f occurs regularly in the expressions of h, p and q. f is then written as

$$f(\zeta) = \omega^2 \sum_{k=0}^{\infty} f_k \zeta^k, \tag{2.18}$$

where

$$f_k = \rho_k - \frac{k_z^2}{\mu\omega^2} B_k^2. \tag{2.19}$$

Using this notation for the coefficients f_k, power series expansions for h and p can be written as

$$h(\zeta) = \omega^2 \sum_{k=0}^{\infty} \Big(r_c^2 f_k + 2 r_c f_{k-1} \mathbf{1}_{k\geq 1} + f_{k-2} \mathbf{1}_{k\geq 2} \Big) \zeta^k, \tag{2.20a}$$

$$p(\zeta) = \zeta\omega^2 \sum_{k=0}^{\infty} \Big(r_c f_k - (k+1) r_c^2 f_{k+1} + (f_{k-1} - 2k r_c f_k) \mathbf{1}_{k\geq 1} + \big(-(k-1) f_{k-1} \big) \mathbf{1}_{k\geq 2} \Big) \zeta^k. \tag{2.20b}$$

The expression for q requires some additional explanation. This is due to the term containing $-k_\perp^2$, which is also expanded. Because of the presence of the slow resonance, at $\zeta = 0$ it holds that $\omega = \omega_C$. Hence $k_\perp$ is unbounded at the resonance position. Like the second derivative of P'_{tr} its power series will then also contain a pole-order term. Constructing the power series for $k_\perp^2$ then starts by taking the power series for v_C^2, v_S^2 and v_A^2. From these, the following derived series can be defined:

$$\omega^2 - \omega_C^2 = \sum_{k=0}^{\infty} c'_k \zeta^k, \tag{2.21a}$$

$$\omega^2 - \omega_S^2 = \sum_{k=0}^{\infty} s'_k \zeta^k, \tag{2.21b}$$

$$\omega^2 - \omega_A^2 = \sum_{k=0}^{\infty} a'_k \zeta^k, \tag{2.21c}$$

$$v_S^2 + v_A^2 = \sum_{k=0}^{\infty} v_k \zeta^k. \tag{2.21d}$$

Using this notation, a power series expansion of $k_\perp^2$ can be constructed. Unlike the previous quantities, for $k_\perp^2$ only a recursive relation for the coefficients can be found. As mentioned before, it should also be noted that this expansion has a term in ζ^{-1}. The expression used is then

$$-k_\perp^2 = \sum_{k=-1}^{\infty} \kappa_k \zeta^k, \tag{2.22}$$

where

$$\kappa_{-1} = \frac{s'_0 a'_0}{v_0 c'_1}, \tag{2.23a}$$

$$\kappa_k = \frac{1}{v_0 c'_1} \left[\sum_{j=0}^{k+1} \sigma_j \alpha_{k-j+1} - \sum_{j=0}^{k} \kappa_{j-1} \left(\sum_{i=0}^{k-j+1} v_i c_{k-j-i+2} \right) \right] \qquad \text{for } k \geq 0. \tag{2.23b}$$

The expansion is made for $-k_\perp^2$ to avoid the minus sign in equation 2.1. Furthermore, these coefficients show the benefit of considering the profiles for the squares of the characteristic speeds instead of those for the speeds themselves. Because only the squares occur in the equation for P'_{tr}, this choice will not cause any problems later on. The expansion of $k_\perp^2$ allows for a series expansion of q, which is then

$$q(\zeta) = \zeta^2\omega^2 \sum_{k=-1}^{\infty} \Bigg[\sum_{j=0}^{k-1} f_j \kappa_{k-j-2} \mathbf{1}_{k\geq 1} + 2r_c \sum_{j=0}^{k} f_j \kappa_{k-j-1} \mathbf{1}_{k\geq 0} + r_c^2 \sum_{j=0}^{k+1} f_j \kappa_{k-j} - m^2 f_k \mathbf{1}_{k\geq 0} \Bigg] \zeta^k. \tag{2.24}$$

With this expression, all parts required to solve equation 2.11 are now available. It is now a matter of substituting equations 2.16, 2.20 and 2.24 into equation 2.11. This yields an equation with on the left-hand side a power series in ζ, including a term in ζ^{-1}. The right-hand side of this equation is still simply zero. To equate these then, it is required that every coefficient of the power series on the left-hand side is itself zero. This is done twice: once for the regular solution, with $A_0 = 1, S_0 = 0$ and once for the singular solution, with $A_0 = 0, S_0 = 1$. The resulting equations can then be solved to yield expressions for the coefficients α_k and σ_k in equation 2.15. Because equation 2.11 is a second-order ordinary differential equation, there are two degrees of freedom. Hence two of the coefficients α_k, σ_k can be chosen freely and without loss of generality. Here it is chosen that $\alpha_0 = \sigma_0 = 1$. The expressions for the coefficients are recursive relations, so starting with a simple expression for the lowest order terms is a natural choice. This effectively leads to the coefficients being normalised with respect to the values of P'_1 and P'_2 at the resonance position. The general recurrence relations are shown in appendix A, where the value of $\alpha_0 = \sigma_0 = 1$ is not substituted in the expressions for higher values of k.

Apart from the coefficients α_k and σ_k, the general expression for P'_{tr} also contains the coupling constant $\mathcal{C}$ that arises in the logarithmic term of P'_2. The value of this constant can be found by equating the pole-order coefficient of the singular solution in equation 2.11 to zero. The result is that the value of $\mathcal{C}$ depends only on the zeroth-order coefficients α_0 and σ_0 of P'_1 and P'_2. Because these can be chosen freely, the value of $\mathcal{C}$ does not depend on the expansion of P'_{tr}. Considering the values $\alpha_0 = \sigma_0 = 1$, the value of $\mathcal{C}$ is found to be

$$\mathcal{C} = -\kappa_{-1}. \tag{2.25}$$

For future calculations, it will be interesting to consider an explicit formula for this value of $\mathcal{C}$. The value of κ_{-1}, which is the pole-order term of $k_\perp^2$ can be found by multiplying $k_\perp^2$ with ζ and subsequently taking the limit of $\zeta \to 0$. To this end, the expansion of $\omega^2 - \omega_C^2$ is considered first. Because $\omega = \omega_C$ at the resonance position, the zeroth-order term c_0 in equation 2.21a will be zero. As a consequence,

$$\lim_{\zeta\to 0} \frac{\omega^2 - \omega_C^2}{\zeta} = c'_1. \tag{2.26}$$

For the other factors in the expression for $k_\perp^2$, the limit of $\zeta \to 0$ can easily be taken, since none of them are zero at the resonance position. The result is then that

$$\begin{aligned}\mathcal{C} &= -\lim_{\zeta\to 0} \frac{(\omega^2-\omega_S^2)(\omega^2-\omega_A^2)}{(v_S^2+v_A^2)\frac{\omega^2-\omega_C^2}{\zeta}} \\ &= -\frac{k_z^4 v_S^4 v_A^4}{(v_S^2+v_A^2)^3 c_1'},\end{aligned} \tag{2.27}$$

where the values of v_S, v_A and ω_C are taken at the resonant position. Because c_1' is the first-order term in a Taylor series expansion, it can be explicitly written as well, which yields

$$c_1' = \left.\frac{d(\omega^2-\omega_C^2)}{d\zeta}\right|_{\zeta=0}. \tag{2.28}$$

With the expressions obtained thus far, it is now possible to find a general dispersion relation for the slow surface wave. This will be the topic of the following section.

2.3 Dispersion relation

The dispersion relation of the slow surface wave relates the frequency ω to the longitudinal wave number k_z. Considering the fundamental mode with $k_z = \pi/L$ thus fixes the frequency by means of this dispersion relation. A dispersion relation in the case of a thin boundary is given by Yu et al. (2017a). To generalise this to the case of arbitrary boundary thickness, the same method as done by Soler et al. (2013) for the Alfvén resonance is considered. In this method, the dispersion relation is derived from the requirement of continuity of P' and ξ_r. This continuity can be expressed by matching the solutions of P' and ξ_r in the boundary layer with the solutions in the external regions. In other words, the following equations must hold:

$$\begin{aligned} P_i'(\zeta_i) &= P_{\rm tr}'(\zeta_i), & P_e'(\zeta_e) &= P_{\rm tr}'(\zeta_e), \\ \xi_{r,i}(\zeta_i) &= \xi_{r,\rm tr}(\zeta_i), & \xi_{r,e}(\zeta_e) &= \xi_{r,\rm tr}(\zeta_e). \end{aligned} \tag{2.29}$$

The solutions in the uniform layers have already been introduced in equations 2.3-2.7. For the solutions in the boundary layer, the same notation is introduced as used by Soler et al. (2013):

$$\mathcal{G}_{i,e} = P_1'(\zeta_{i,e}), \tag{2.30a}$$

$$\mathcal{F}_{i,e} = P_2'(\zeta_{i,e}), \tag{2.30b}$$

$$\Xi_{i,e} = \frac{1}{\rho(\zeta_{i,e})(\omega^2-\omega_A^2(\zeta_{i,e}))}\frac{dP_1'}{d\zeta}(\zeta_{i,e}), \tag{2.30c}$$

$$\Gamma_{i,e} = \frac{1}{\rho(\zeta_{i,e})(\omega^2-\omega_A^2(\zeta_{i,e}))}\frac{dP_2'}{d\zeta}(\zeta_{i,e}), \tag{2.30d}$$

where the double subscript i, e denotes that both the internal and the external values can be used in the expressions. $\mathcal{G}$ and $\mathcal{F}$ are the values of P_1' and P_2', respectively, at the edges of the boundary layer. Ξ and Γ are then the corresponding expressions for ξ_r, where Ξ is the value if P_1' is considered instead of $P_{\rm tr}'$ and Γ the value if P_2' is considered instead of $P_{\rm tr}'$. In this notation, the conditions of continuity can be rewritten as

$$A_i I_m(k_{\perp,i}(R - l/2)) = A_0\mathcal{G}_i + S_0\mathcal{F}_i, \tag{2.31a}$$
$$A_e K_m(k_{\perp,e}(R + l/2)) = A_0\mathcal{G}_e + S_0\mathcal{F}_e, \tag{2.31b}$$
$$\frac{A_i k_{\perp,i}}{\rho_i(\omega^2 - \omega_{Ai}^2)} I_m'(k_{\perp,i}(R - l/2)) = A_0\Xi_i + S_0\Gamma_i, \tag{2.31c}$$
$$\frac{A_e k_{\perp,e}}{\rho_e(\omega^2 - \omega_{Ae}^2)} K_m'(k_{\perp,e}(R + l/2)) = A_0\Xi_e + S_0\Gamma_e. \tag{2.31d}$$

This is a linear, homogeneous system of four equations in the four unknowns A_i, A_e, A_0 and S_0 that arise in the expressions of $P_{\rm tr}'$. Because the system is homogeneous, the only way a non-trivial solution can exist is if its determinant is zero. This condition gives the dispersion relation in the form

$$\begin{vmatrix} I_m(k_{\perp,i}(R-l/2)) & 0 & -\mathcal{G}_i & -\mathcal{F}_i \\ 0 & K_m(k_{\perp,e}(R+l/2)) & -\mathcal{G}_e & -\mathcal{F}_e \\ \frac{k_{\perp,i}}{\rho_i(\omega^2-\omega_{Ai}^2)} I_m'(k_{\perp,i}(R-l/2)) & 0 & -\Xi_i & -\Gamma_i \\ 0 & \frac{k_{\perp,e}}{\rho_e(\omega^2-\omega_{Ae}^2)} K_m'(k_{\perp,e}(R+l/2)) & -\Xi_e & -\Gamma_e \end{vmatrix} = 0. \tag{2.32}$$

This determinant can be calculated to give the dispersion relation in a more useful form. The result is that we can write it as

$$\frac{\frac{k_{\perp,e}}{\rho_e(\omega^2-\omega_{Ae}^2)}\frac{K_m'(k_{\perp,e}(R+l/2))}{K_m(k_{\perp,e}(R+l/2))}\mathcal{G}_e - \Xi_e}{\frac{k_{\perp,e}}{\rho_e(\omega^2-\omega_{Ae}^2)}\frac{K_m'(k_{\perp,e}(R+l/2))}{K_m(k_{\perp,e}(R+l/2))}\mathcal{F}_e - \Gamma_e} - \frac{\frac{k_{\perp,i}}{\rho_i(\omega^2-\omega_{Ai}^2)}\frac{I_m'(k_{\perp,i}(R-l/2))}{I_m(k_{\perp,i}(R-l/2))}\mathcal{G}_i - \Xi_i}{\frac{k_{\perp,i}}{\rho_i(\omega^2-\omega_{Ai}^2)}\frac{I_m'(k_{\perp,i}(R-l/2))}{I_m(k_{\perp,i}(R-l/2))}\mathcal{F}_i - \Gamma_i} = 0. \tag{2.33}$$

This is the general form of the dispersion relation. Remember that so far, no value of the thickness l has been imposed yet. Similarly, the actual profiles of all plasma parameters have not yet been imposed, meaning that this dispersion relation has not lost any generality. A comparison of this equation can now be made with the dispersion relation found by Yu et al. (2017a), who studied the cusp resonance in the TB limit. To this end, the limit of $l/R \approx 0$ is imposed on equation 2.33. In this limit, it always holds that $r \approx r_c$ within the boundary layer, since this layer is where the resonant position is situated. It is then clear that $\zeta \approx 0$. It is thus possible to approximate all power series by their term of lowest order in ζ. This has an effect on the values of the parameters $\mathcal{G}, \mathcal{F}, \Xi$ and Γ. All of these will be approximated to zeroth-order to obtain the results in the TB limit. Because the lowest order term of P_1' is a linear term, it follows that in the TB limit

$$\mathcal{G}_{i,e} \approx 0. \tag{2.34}$$

In the definition of P_2', the logarithmic term is multiplied with P_1'. For small values of ζ, this term will then always be zero. As a result, P_2' is approximated in the TB limit by σ_0, which was chosen to be equal to 1. Thus,

$$\mathcal{F}_{i,e} \approx 1. \tag{2.35}$$

For the approximation of Ξ, the derivative of P_1' is considered. For small values of ζ, it is clear that this derivative can be approximated by α_0, which is also equal to 1. The derivative is then divided by $\rho(\omega^2 - \omega_A^2)$. The approximation up to zeroth-order of this term in the TB limit is simply the evaluation of this expression at the resonance position. In other words,

$$\Xi_{i,e} \approx \frac{1}{\rho_0(\omega_C^2 - \omega_A^2)}, \tag{2.36}$$

with the frequencies evaluated at $r = r_C$. The factor between brackets is a_0 in the notation of equation 2.21c. Finally, Γ is considered. The denominator in this expression is the same as for Ξ. For the numerator, the derivative of P_2' is considered. The first term of this derivative can be approximated by σ_1, which is 0, as can be seen in appendix A. The derivative of the product of P_1' with $\ln(\zeta)$ can be approximated by $1 + \ln(\zeta)$ up to zeroth order. This means that

$$\Gamma_{i,e} \approx \frac{\mathcal{C}(1 + \ln(\zeta_{i,e}))}{\rho_0(\omega_C^2 - \omega_A^2)}. \tag{2.37}$$

With these approximations, the dispersion relation can be reduced in the TB limit to

$$\frac{k_{\perp,e}}{\rho_e(\omega^2 - \omega_{Ae}^2)} \frac{K_m'(k_{\perp,e}R)}{K_m(k_{\perp,e}R)} - \frac{k_{\perp,i}}{\rho_i(\omega^2 - \omega_{Ai}^2)} \frac{I_m'(k_{\perp,i}R)}{I_m(k_{\perp,i}R)} = \frac{\mathcal{C}\ln(\zeta_e/\zeta_i)}{\rho_0 k_z^2 \frac{v_A^4}{c^2 + v_A^2}}, \tag{2.38}$$

where further $\omega_C^2 - \omega_A^2$ has been expanded as $k_z^2 v_A^4/(v_S^2 + v_A^2)$. The dispersion relation can be further reduced by introducing the same notation as Yu et al. (2017a):

$$Q_m = \frac{I_m'(k_{\perp,i}R)K_m(k_{\perp,e}R)}{I_m(k_{\perp,i}R)K_m'(k_{\perp,e}R)}, \tag{2.39a}$$

$$G_m = \frac{K_m(k_{\perp,e}R)}{K_m'(k_{\perp,e}R)}. \tag{2.39b}$$

With these notations, the dispersion relation can again be rewritten as

$$\rho_i(\omega^2 - \omega_{Ai}^2) - \rho_e(\omega^2 - \omega_{Ae}^2)\frac{k_{\perp,i}}{k_{\perp,e}} Q_m = \frac{\mathcal{C}\ln(\zeta_e/\zeta_i)}{\rho_0 k_z^2 \frac{v_A^4}{c^2 + v_A^2}} \rho_i \rho_e (\omega^2 - \omega_{Ai}^2)(\omega^2 - \omega_{Ae}^2)\frac{G_m}{k_{\perp,e}}. \tag{2.40}$$

One final remark should be made regarding this equation. In the TB assumption it holds that $r_c \approx R$, which means that $\zeta_e \approx l/2$ and $\zeta_i \approx -l/2$. As such, the ratio ζ_e/ζ_i that

appears in this equation is approximately -1. This negative term arises as the argument of the logarithm in the equation and thus needs to be dealt with. To this end, the complex logarithm is defined as making a jump of $\pm i\pi$ when the argument crosses the negative real axis. This allows for a further rewrite of the dispersion relation. Using the expression found earlier for $\mathcal{C}$ and keeping the sign of c_1 in mind, a positive sign is taken for the jump and the expression $\ln(\zeta_e/\zeta_i)$ is approximated as $i\pi$ in the TB limit. This reasoning is equivalent to the reasoning done by Soler et al. (2013) for the case of Alfvén resonance. With this definition, and by substituting the expression for $\mathcal{C}$, the dispersion relation in the TB limit is finally written as

$$\rho_i(\omega^2-\omega_{Ai}^2)-\rho_e(\omega^2-\omega_{Ae}^2)\frac{k_{\perp,i}}{k_{\perp,e}}Q_m=\frac{i\pi k_z^2}{\rho_0|c_1'|}\left(\frac{v_S^2}{v_S^2+v_A^2}\right)^2\rho_i\rho_e(\omega^2-\omega_{Ai}^2)(\omega^2-\omega_{Ae}^2)\frac{G_m}{k_{\perp,e}}. \tag{2.41}$$

This is precisely the dispersion relation found by Yu et al. (2017a), who used the notation Δ_c for c_1'. This result shows that the calculations made so far consistently revert to previously known results in the case of a thin boundary. These results are more general, however, and do not rely on the assumption of a small boundary thickness. Up to this point, the specific profiles of plasma parameters within the boundary layer has not yet been considered. The next chapter will consist of a numerical study of these results, where the specific form of the profiles will be of importance.

Chapter 3

Numerical study

3.1 Parameter profiles

3.1.1 General method

In this chapter, a numerical study of the cusp resonance studied so far is performed. The method used is the same as the one used by Soler et al. (2013) for the Alfvén resonance. However, as will be shown, simply copying this method for the slow resonance is not possible, as the study for the cusp resonance has additional complications that do not arise in the case of Alfvén resonance. In this first section, the general methodology is explained. The later sections will then aim to explain the limitations of this method and propose a possible solution to fix this. However, these are only suggestions and a full solution is not reached.

For the following study, numerical values for the parameters are needed. As mentioned before, the present study is concerned with the study of a magnetic pore. The values used for this are obtained from Grant et al. (2015), based on observations using the Dunn Space Telescope. In the internal region of the cylinder, these values are $v_{Si} = 7$ km/s, $v_{Ai} = 12$ km/s and $v_{Ci} = 6.0464$ km/s. The corresponding values for the exterior region are then $v_{Se} = 11.5$ km/s, $v_{Ae} = 0$ km/s and $v_{Ce} = 0$ km/s. This corresponds to the limit of $\beta \to \infty$ within the exterior region, which is the background photosphere. This environment does indeed have a magnetic field which is several orders of magnitude lower than that of the inside of the pore, which makes the taking of this limit a valid approximation. Within the boundary layer, these values are then connected continuously. From the values of the characteristic speeds, the values of density, magnetic field strength and thermal pressure can then be found by inverting equations 1.4. This results in

$$B^2 = \frac{\gamma P v_A^2}{\frac{v_S^2}{\mu} + \frac{\gamma}{2\mu} v_A^2}, \qquad \rho = \frac{B^2}{\mu v_A^2}, \qquad p_{\text{th}} = P - \frac{B^2}{2\mu}. \tag{3.1}$$

Here P is the total pressure, which is constant in the entirety of the system. Again, because the photosphere consists mostly of hydrogen, a value of 5/3 is considered for the adiabatic index γ. The magnetic permeability μ has a value of $4\pi \cdot 10^{-4}$ H/km. The internal and external values of these parameters are also connected continuously within the boundary layer, in such a way that these relations hold at every point within this layer. These relations are the analytic expressions, which will be approximated by Taylor

series, as explained in chapter 2. For numerical purposes, these Taylor series must be truncated at a certain point $k_{\max}$, which defines the desired accuracy. In general, the Taylor series considered here will be truncated at $k_{\max} = 50$, which guarantees a very good approximation of the analytical expression.

In order to perform an in-depth study of the slow resonance, the dispersion relation 2.33 needs to be solved for the frequency ω. This cannot be done analytically, since ω appears in the coefficients of P'_{tr} and thus in all of the parameters $\mathcal{G}$, $\mathcal{F}$, Ξ and Γ. Hence, the dispersion relation is solved numerically through an iterative process. For this process, at first the entire slow continuum is considered: this is the set of all values for the slow frequency. In the case of the magnetic pore conditions considered here, the slow continuum is $[\omega_{Ce}, \omega_{Ci}]$. Then the method consists of iteratively varying the frequency ω within this interval and checking at each such iteration the value of the dispersion function, which is the left-hand side of equation 2.33. Based on the values obtained in these iterations, the search interval is then progressively refined until a sufficiently accurate value is found for ω, for which the dispersion function is sufficiently close to zero.

Apart from the frequency ω, also the position of the resonance r_c arises in the expansion coefficients of P'_{tr}. These two parameters are entirely dependent on one another through the consistency requirement that $\omega = \omega_C$ at $r = r_c$, which simply means that the resonance happens at the resonant point. Specifying a value of ω within the slow continuum then also fixes the corresponding value of r_c to the position where the cusp frequency is equal to ω, and vice versa. It is thus also possible to vary r_c within the boundary layer. As will be explained in the next paragraph, the profile of the cusp frequency is one-to-one so varying r_c instead of ω does not change the method in general. The advantage of changing r_c is that its value provides a more visual interpretation of each iteration than the corresponding value of ω does.

There are six different parameters for which profiles are considered: the cusp, sound and Alfvén speeds, the density, magnetic field and the thermal pressure. Because at every point within the considered domain equations 1.4 and 3.1 must hold, it is only necessary to specify the profiles of two of these six parameters: the profiles of the other four can then be derived from these equations. A choice must then be made regarding which two parameters are chosen to be defined first. One of these two must be the cusp speed. This is because the Frobenius method used in chapter 2 assumes that there is only one resonant point. There can thus be only one position where the frequency is equal to the cusp frequency, which is proportional to the cusp speed. If the profile for the cusp speed is not one-to-one, it is possible that there are multiple such positions. Hence the cusp speed should be specified upfront, to guarantee that it is one-to-one. Of course, physically it is possible that v_C has a profile which is not one-to-one. Yu et al. (2017b) show that in this case the resonance is situated in one of the a priori possible resonance points. However, the general Frobenius method has no way of determining which of these points will contain the be the ultimate resonance point, so this possibility is not investigated further. The second parameter to be specified can then be chosen freely. For the following calculations, it is assumed that the sound speed is the other parameter which is specified upfront. The Alfvén speed, density, magnetic field and thermal pressure are then derived from these two, where the formula for the Alfvén speed can be found from equation 1.4 to be

$$v_A^2 = \frac{v_S^2 v_C^2}{v_S^2 - v_C^2}. \tag{3.2}$$

The other parameters can simply be found from equation 3.1. An interesting question is how the Taylor series of v_A^2, ρ, B^2 and p_{th} can best be constructed from those of v_S^2 and v_C^2. As can be seen from equations 3.1 and 3.2, products and quotients of parameters arise regularly in these expressions. One option would be to calculate the terms of the derived series directly from the terms of the given series. This is done as follows: given two power series

$$f = \sum_{k=0}^{\infty} f_k \zeta^k \qquad \text{and} \qquad g = \sum_{k=0}^{\infty} g_k \zeta^k, \tag{3.3}$$

the power series of fg can be constructed by multiplying these two series and sorting the terms by degree of ζ to obtain again a power series in ζ. Writing the coefficient of degree k in this product series as $(fg)_k$, the following formula can be found:

$$(fg)_k = \sum_{j=0}^{k} f_j g_{k-j}. \tag{3.4}$$

Similarly, a formula can be found for the coefficients of the reciprocal of a power series. Starting from the coefficients of f, the aim is to construct a power series for $1/f$. Unlike the terms of the product series, this time only a recursive relation can be found for the terms. Writing the coefficient of degree k in this series as $(1/f)_k$, the relation found is

$$\begin{aligned} \left(\frac{1}{f}\right)_0 &= \frac{1}{f_0}, \\ \left(\frac{1}{f}\right)_k &= -\frac{\sum_{j=1}^{k} f_j \left(\frac{1}{f}\right)_{k-j}}{f_0}. \end{aligned} \tag{3.5}$$

In these expressions it is assumed that $f_0 \neq 0$, otherwise the reciprocal of f is not defined at $\zeta = 0$ so a power series is impossible to construct. With the formulas for Taylor series of the product and reciprocal, Taylor series for all parameters can be constructed from the series for v_C^2 and v_S^2. However, calculating the coefficients in this manner is not numerically stable. An illustration of this instability is shown in figure 3.1, where the coefficients of B^2 are calculated according to this method. Clearly, for values of k higher than 20 the coefficients diverge, making this method not useful for considering high orders of accuracy. For comparison, an analytic calculation of the coefficients is plotted together with the numerically calculated ones. For low degrees of k both methods show the same values, but for higher degrees only the analytic method is valid. Hence, calculating the coefficients of the derived series directly from the coefficients of the other series is not a good approach. Instead, the analytic expressions of the derived parameters will be calculated first, and the Taylor series will then be constructed from these formulas. This method has the downside that it is less flexibly adapted to different profiles and that

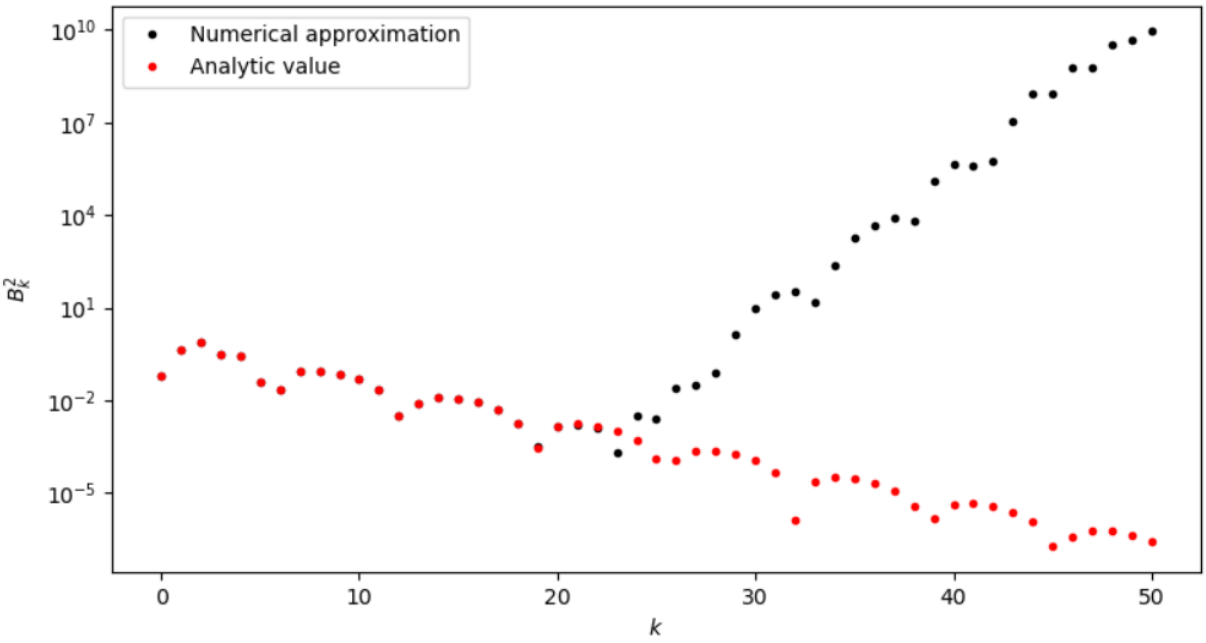

Figure 3.1: Comparison of an analytical and numerical calculation for the coefficients in the power series expansion of B^2. For low values of the degree k both methods agree, but the numerical method becomes unstable as k grows. The value of the coefficients is based on a sinusoidal profile for v_C^2 and v_S^2.

more complicated profiles may not be easily adapted at all. The upside is that this more analytical approach is much more stable, since an explicit formula for all coefficients can be constructed. In the rest of this section, two profiles will be studied: a linear profile and a sinusoidal profile.

3.1.2 Linear profile

The simplest possible profile that can be considered for the nonuniform layer is a linear one. This linear profile is considered specifically for the squares of the cusp and sound speeds. The other parameters then have profiles which are derived from these two, which will not be linear. When one of these derived profiles is referred to as linear, this will always mean that it is derived from the linear profile for the squares of cusp and sound speed, not that the profile itself is linear. This is to easily distinguish from the sinusoidal profiles that are studied next. To find expressions for all profiles, some notation is introduced:

$$\widetilde{v_C^2} = \frac{v_{Ce}^2 - v_{Ci}^2}{l}, \qquad \widehat{v_C^2} = \left(\frac{1}{2} + \frac{R}{l}\right) v_{Ci}^2 + \left(\frac{1}{2} - \frac{R}{l}\right) v_{Ce}^2, \tag{3.6a}$$

$$\widetilde{v_S^2} = \frac{v_{Se}^2 - v_{Si}^2}{l}, \qquad \widehat{v_S^2} = \left(\frac{1}{2} + \frac{R}{l}\right) v_{Si}^2 + \left(\frac{1}{2} - \frac{R}{l}\right) v_{Se}^2. \tag{3.6b}$$

In this notation, the profiles for sound and cusp speed in the boundary layer can be very simply written as

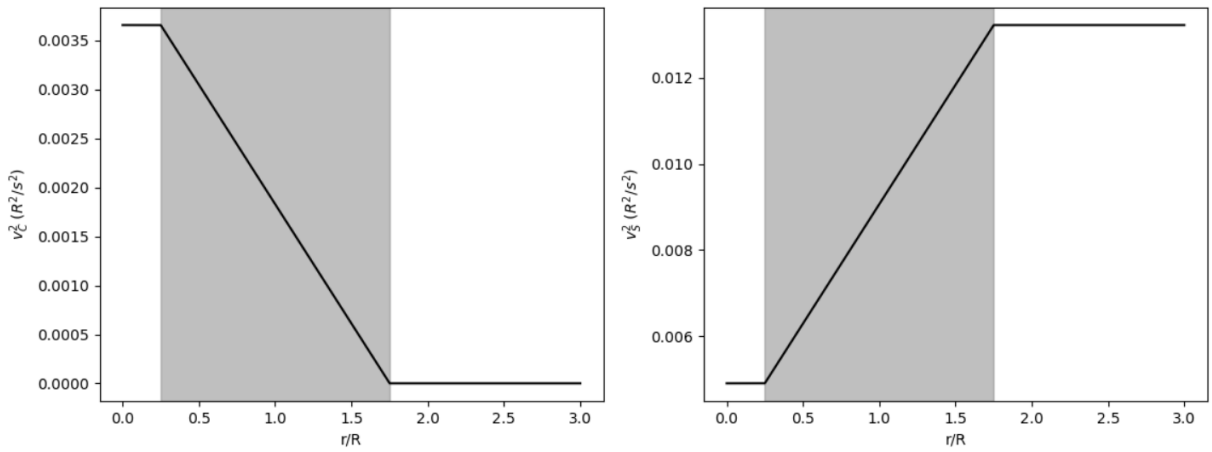

Figure 3.2: Linear profiles for the squares of cusp and sound speed. The gray region represents the nonuniform boundary layer which is defined here for $l/R = 1.5$. Outside this region the profiles are constant. All distances are normalised with respect to the cylinder radius R.

$$v_C^2 = \widetilde{v_C^2} r + \widehat{v_C^2}, \tag{3.7a}$$
$$v_S^2 = \widetilde{v_S^2} r + \widehat{v_S^2}. \tag{3.7b}$$

By defining $\widetilde{v_{C,S}^2}$ and $\widehat{v_{C,S}^2}$ as in equation 3.6, these profiles guarantee that the sound and cusp speeds are continuous in the entire domain. It can be easily checked that at $r = R - l/2$ these profiles give the interior value of the speeds and at $r = R + l/2$ they give the exterior value. It should be noted that these profiles are given in the variable r instead of ζ. To construct the power series from them, the transformation $r = \zeta + r_c$ still needs to be considered. Performing this transformation, it is easy to see that the coefficients in the series expansion are

$$\left(v_C^2\right)_0 = \widetilde{v_C^2} r_c + \widehat{v_C^2}, \qquad \left(v_C^2\right)_1 = \widetilde{v_C^2}, \qquad \left(v_C^2\right)_k = 0 \text{ if } k \geq 2, \tag{3.8a}$$
$$\left(v_S^2\right)_0 = \widetilde{v_S^2} r_c + \widehat{v_S^2}, \qquad \left(v_S^2\right)_1 = \widetilde{v_S^2}, \qquad \left(v_S^2\right)_k = 0 \text{ if } k \geq 2. \tag{3.8b}$$

Throughout this chapter, the notation $(f)_k$ will denote the coefficient in the Taylor series of any parameter f corresponding to ζ^k. These linear profiles are shown in figure 3.2. From equations 3.8 it is clear that as the resonant position changes, the profiles remain the same, hence this formula can be used in any iteration to construct a linear profile which is expanded around the resonant position. From the profiles for the cusp and sound speeds a profile can then be constructed for the square of the Alfvén speed as well. A fairly straightforward calculation yields that

$$v_A^2 = \frac{\widetilde{v_S^2}\widetilde{v_C^2}}{\widetilde{v_S^2} - \widetilde{v_C^2}} r + \frac{\widehat{v_C^2}\left(\widetilde{v_S^2}\right)^2 - \widehat{v_S^2}\left(\widetilde{v_C^2}\right)^2}{\left(\widetilde{v_S^2} - \widetilde{v_C^2}\right)^2} + \frac{\left(\frac{\widehat{v_C^2}\widetilde{v_S^2} - \widehat{v_S^2}\widetilde{v_C^2}}{\widetilde{v_S^2} - \widetilde{v_C^2}}\right)^2}{(\widetilde{v_S^2} - \widetilde{v_C^2})r + \widehat{v_S^2} - \widehat{v_C^2}}. \tag{3.9}$$

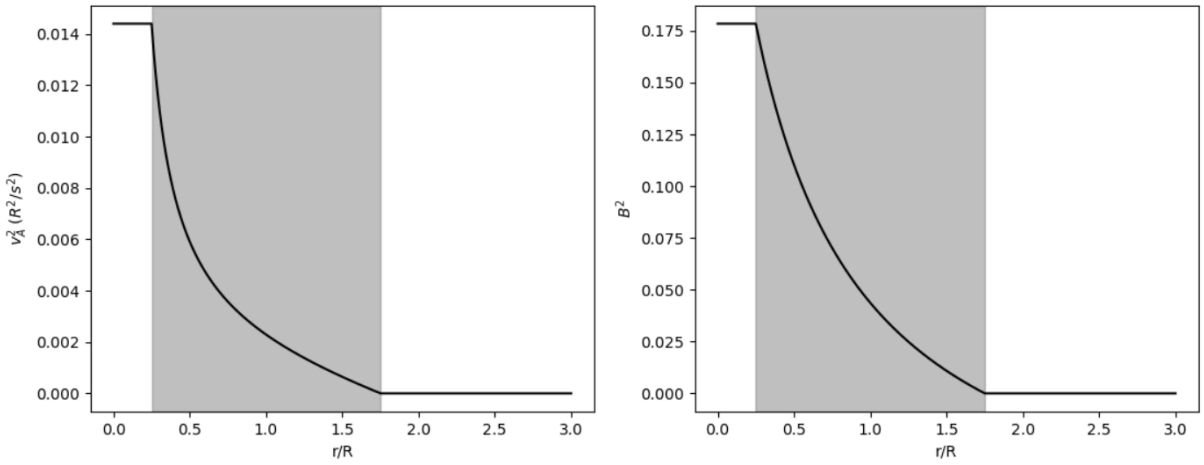

Figure 3.3: Profiles for the squares of the Alfvén speed and magnetic field strength, based on linear profiles for the squares of cusp and sound speed. Again, $l/R = 1.5$ and all distances are normalised with respect to the cylinder radius R. Values of B^2 are normalised with respect to P.

The first two terms in this expression describe a linear function in r. The third term is rational however, which means that this function has a pole. Because within the boundary layer v_S and v_C are nowhere equal, this pole will lie outside the boundary layer. The precise position depends on the thickness which is chosen. For a value of $l/R = 1.5$ as is chosen in e.g. figure 3.2, the boundary layer spans the region of $[0.25R, 1.75R]$ and the pole would be situated at $r = 0.09R$, which is in the interior region. Regardless of the value of l, this pole never lies in the boundary layer, so v_A^2 is properly defined in the entire domain, since in the interior and exterior regions a constant value is imposed. However, the presence of this pole will cause the convergence radius of the Taylor series to be limited, which will be further investigated later.

Postponing the discussion of the convergence radius, the general Taylor series for v_A^2 within the convergence disk can be constructed. The terms in the expression can be simply converted to Taylor series coefficients as before, where the transformation $r = \zeta + r_c$ must be considered. The result is that the Taylor series of v_A^2 can be written as

$$T_{v_A^2}(\zeta) = \frac{\widetilde{v_S^2}\widetilde{v_C^2}}{\widetilde{v_S^2} - \widetilde{v_C^2}}\zeta + \frac{\widetilde{v_S^2}\widetilde{v_C^2}}{\widetilde{v_S^2} - \widetilde{v_C^2}}r_c + \frac{\widehat{v_C^2}\left(\widetilde{v_S^2}\right)^2 - \widehat{v_S^2}\left(\widetilde{v_C^2}\right)^2}{\left(\widetilde{v_S^2} - \widetilde{v_C^2}\right)^2} + \frac{\left(\frac{\widehat{v_C^2}\widetilde{v_S^2} - \widehat{v_S^2}\widetilde{v_C^2}}{\widetilde{v_S^2} - \widetilde{v_C^2}}\right)^2}{(\widetilde{v_S^2} - \widetilde{v_C^2})r_c + \widehat{v_S^2} - \widehat{v_C^2}} \sum_{k=0}^{\infty} \left(-\frac{\widetilde{v_S^2} - \widetilde{v_C^2}}{(\widetilde{v_S^2} - \widetilde{v_C^2})r_c + \widehat{v_S^2} - \widehat{v_C^2}}\right)^k \zeta^k. \tag{3.10}$$

With the profiles of the sound, cusp and Alfvén speeds, it is now possible to construct profiles for the magnetic field, density and thermal pressure. These can be found from equations 3.1. To keep these expressions simple, some extra notation is introduced:

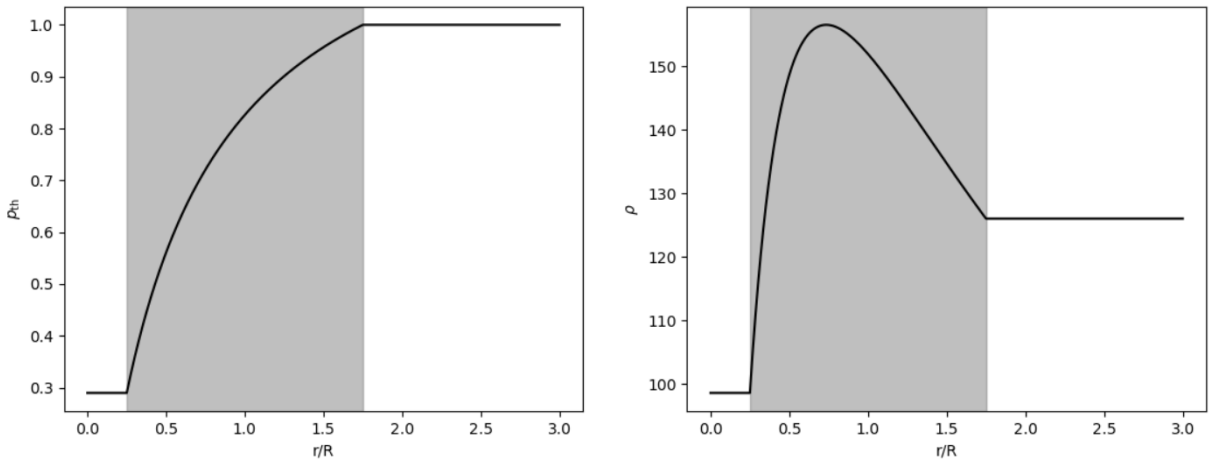

Figure 3.4: Profiles for the thermal pressure and density, based on linear profiles for the squares of cusp and sound speed. Again, $l/R = 1.5$ and all distances are normalised with respect to the cylinder radius R. Values of p_{th} are normalised with respect to P.

$$V_1 = \frac{1}{\mu}\left(\widehat{v_S^2} - \frac{\widehat{v_C^2}\widetilde{v_S^2}}{\widetilde{v_C^2}}\right), \tag{3.11a}$$

$$V_2 = \frac{1}{\mu}\left(\frac{\widetilde{v_S^2}}{\widetilde{v_C^2}} - 1 + \frac{\gamma}{2}\right). \tag{3.11b}$$

Now the magnetic field can be written as

$$B^2 = \frac{\gamma P}{V_2}\left(1 - \frac{V_1}{\widetilde{v_C^2}V_2 r + V_1 + \widehat{v_C^2}V_2}\right). \tag{3.12}$$

Like the Alfvén speed, this formula also contains a rational function. Again, the pole of this rational function does not lie within the boundary layer but its presence will cause the convergence radius to be limited. Plots of the profiles of v_A^2 and B^2 can be found in figure 3.3. Within the region where it is convergent, the Taylor series of B^2 can be written as

$$T_{B^2}(\zeta) = \frac{\gamma P}{V_2} - \frac{\gamma P \frac{V_1}{V_2}}{\widetilde{v_C^2}V_2 r_c + V_1 + \widehat{v_C^2}V_2}\sum_{k=0}^{\infty}\left(-\frac{\widetilde{v_C^2}V_2}{\widetilde{v_C^2}V_2 r_c + V_1 + \widehat{v_C^2}V_2}\right)^k \zeta^k. \tag{3.13}$$

Now only the profiles of density and thermal pressure remain. From equation 3.1 it is clear that the formula for p_{th} can be very easily derived by dividing the expression for B^2 by -2μ and adding the total pressure. Because the total pressure is a constant, the coefficients of the resulting Taylor series for p_{th} are simply scalar multiples of those of T_{B^2}, with P added to the zeroth-order term. For completeness, the expression for p_{th} and its Taylor series $T_{p_{\mathrm{th}}}$ are given here:

$$p_{\mathrm{th}} = P + \frac{\gamma P}{2\mu V_2}\left(\frac{V_1}{\widetilde{v_C^2}V_2 r + V_1 + \widehat{v_C^2}V_2} - 1\right), \tag{3.14}$$

$$T_{p_{\text{th}}}(\zeta) = P - \frac{\gamma P}{2\mu V_2} + \frac{\gamma P \frac{V_1}{2\mu V_2}}{\widetilde{v_C^2} V_2 r_c + V_1 + \widehat{v_C^2} V_2} \sum_{k=0}^{\infty} \left(-\frac{\widetilde{v_C^2} V_2}{\widetilde{v_C^2} V_2 r_c + V_1 + \widehat{v_C^2} V_2} \right)^k \zeta^k. \tag{3.15}$$

Finally, the profile for the density is considered. Again from equation 3.1, it can be calculated to be

$$\rho = \frac{\gamma P}{\mu} \frac{\left(\widetilde{v_S^2} - \widetilde{v_C^2}\right) r + \widehat{v_S^2} - \widehat{v_C^2}}{\widetilde{v_S^2}\widetilde{v_C^2} V_2 r^2 + \left(\widetilde{v_S^2} V_1 + \widehat{v_C^2}\widetilde{v_S^2} V_2 + \widehat{v_S^2}\widetilde{v_C^2} V_2\right) r + \widehat{v_S^2} V_1 + \widehat{v_C^2}\widehat{v_S^2} V_2}. \tag{3.16}$$

The resulting equation is again a rational function, which this time has two poles. As can be seen from figure 3.4, this profile is not one-to-one. As mentioned before, depending on which two parameters are chosen first, a different parameter can yield a profile which is not one-to-one. This is an illustration that backs the choice of specifying the cusp speed first. The profile for ρ has two poles, which are found at

$$\begin{aligned} r_{1,2} = \frac{1}{2\widetilde{v_S^2}\widetilde{v_C^2} V_2} \Bigg[& - \left(\widetilde{v_S^2} V_1 + \widehat{v_C^2}\widetilde{v_S^2} V_2 + \widehat{v_S^2}\widetilde{v_C^2} V_2\right) \\ & \pm \sqrt{\left(\widetilde{v_S^2} V_1 + \widehat{v_C^2}\widetilde{v_S^2} V_2 + \widehat{v_S^2}\widetilde{v_C^2} V_2\right)^2 - 4\widetilde{v_S^2}\widetilde{v_C^2} V_2 \left(\widehat{v_S^2} V_1 + \widehat{v_C^2}\widehat{v_S^2} V_2\right)} \Bigg]. \end{aligned} \tag{3.17}$$

Neither of these poles lie within the boundary layer. For the values considered in this study, both are found for values of $r < R - l/2$. This means that, again, the profile is well defined within the boundary layer but the presence of the pole will cause a smaller convergence radius. Since both poles lie at positions $r < R - l/2$, the pole at the largest value of r will determine the size of the convergence radius. With these two poles determined, the Taylor series of ρ within the convergence disk can be written as

$$\begin{aligned} T_\rho = \frac{\gamma P}{\mu \widetilde{v_C^2}\widetilde{v_S^2} V_2} \Bigg[& \frac{\left(\widetilde{v_S^2} - \widetilde{v_C^2}\right) r_1 + \widehat{v_S^2} - \widehat{v_C^2}}{(r_c - r_1)(r_1 - r_2)} \sum_{k=0}^{\infty} \left(\frac{-1}{r_c - r_1}\right)^k \zeta^k \\ & + \frac{\left(\widetilde{v_S^2} - \widetilde{v_C^2}\right) r_2 + \widehat{v_S^2} - \widehat{v_C^2}}{(r_c - r_2)(r_2 - r_1)} \sum_{k=0}^{\infty} \left(\frac{-1}{r_c - r_2}\right)^k \zeta^k \Bigg]. \end{aligned} \tag{3.18}$$

This concludes the list of profiles and Taylor series for all parameters in the case of a linear profile for the cusp and sound speeds. In the next section, a similar derivation will be made for the case of sinusoidal profiles for v_C^2 and v_S^2. The rest of this chapter will then focus on the numerical aspects of implementing these profiles, where it will be shown that the limited convergence radii for these parameters do indeed pose a significant problem for solving the dispersion relation.

3.1.3 Sinusoidal profile

A linear profile is the simplest possible profile that can be considered for the nonuniform region. However, it has a few downsides. Perhaps the most obvious of these is that it gives rise to rational functions in the derived profiles. These rational functions may not have their poles within the boundary layer itself, but they are close enough to influence the convergence radius of the corresponding Taylor series. An attempt can be made at fixing this problem by considering a different profile. To this end, a sinusoidal profile is considered here for the squares of the sound and cusp speed. To study these profiles, again some new notation is introduced:

$$\overline{v_C^2} = \frac{v_{Ce}^2 + v_{Ci}^2}{2}, \qquad \underline{v_C^2} = \frac{v_{Ce}^2 - v_{Ci}^2}{2}, \tag{3.19a}$$

$$\overline{v_S^2} = \frac{v_{Se}^2 + v_{Si}^2}{2}, \qquad \underline{v_S^2} = \frac{v_{Se}^2 - v_{Si}^2}{2}. \tag{3.19b}$$

The sinusoidal profiles are then constructed in such a way that the boundary layer spans exactly one half of a period. This guarantees that the profile is one-to-one and that the heights of the top and crest of the sine wave correspond to the values in the interior and exterior regions. This not only makes the profile itself continuous, but also its derivative, resulting in a smoother profile than the linear case. Using the notation in equation 3.19, the profiles of cusp and sound speed can be written as

$$v_C^2 = \overline{v_C^2} + \underline{v_C^2} \sin\left(\frac{\pi}{l}(r - R)\right), \tag{3.20a}$$

$$v_S^2 = \overline{v_S^2} + \underline{v_S^2} \sin\left(\frac{\pi}{l}(r - R)\right). \tag{3.20b}$$

These profiles are shown in figure 3.5. Here it can be clearly seen that the nonuniform layer spans exactly one half period. The sinusoidal profiles are similar in shape to the linear ones, where the main difference is that the sinusoidal profiles are smooth at the edges of the boundary layer. Now, Taylor series will be constructed for these profiles and for those of v_A^2, ρ, B^2 and p_{th}. The method will be somewhat different from before: because the sinusoidal profiles are more complicated, especially taking derivatives of the profiles is less straightforward. Therefore, the coefficients of the Taylor series will be calculated from the coefficients of v_S^2 and v_C^2 themselves, which can still be easily found. Unlike the purely numerical method explained in the beginning of this chapter, this will still be based on analytic profiles of the parameters. Hence this method is still more stable than the numerical method which used several intermediary steps to obtain coefficients, leading to an unstable result.

First the Taylor series for the squares of sound and cusp speed are constructed. For this, the Taylor series of the sine function is considered. This is written as

$$\sin\left(\frac{\pi}{l}(r - R)\right) = \sin\left(\frac{\pi}{l}(\zeta + r_c - R)\right) = \sum_{k=0}^{\infty} s_k \zeta^k. \tag{3.21}$$

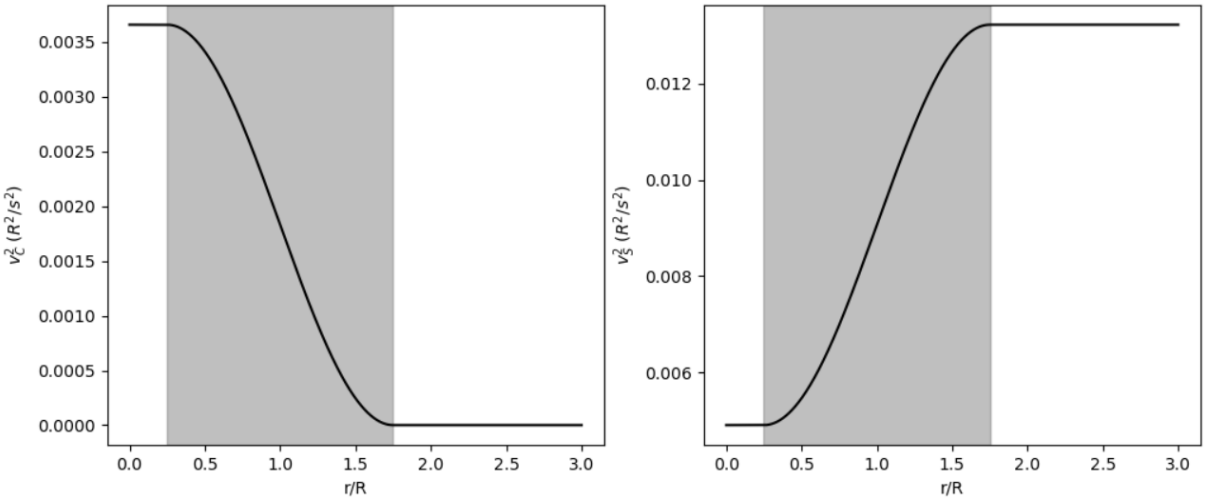

Figure 3.5: Sinusoidal profiles for the squares of cusp and sound speed. Similar to before, the gray region represents the nonuniform boundary layer, which is again defined for $l/R = 1.5$. All distances are normalised with respect to the cylinder radius R.

The coefficients in the Taylor series of sin are well known, so s_k can be calculated easily. The general formula is

$$s_k = \frac{(-1)^{\lfloor k/2 \rfloor}}{k!} \left(\frac{\pi}{l}\right)^k \left[\sin\left(\frac{\pi}{l}(r_c - R)\right) \mathbf{1}_{k\equiv 0 \mathrm{mod} 2} + \cos\left(\frac{\pi}{l}(r_c - R)\right) \mathbf{1}_{k\equiv 1 \mathrm{mod} 2}\right]. \tag{3.22}$$

It is then very simple to obtain the coefficients in the expansions of v_C^2 and v_S^2:

$$(v_C^2)_k = \underline{v_C^2} s_k + \overline{v_C^2} \mathbf{1}_{k=0}, \tag{3.23a}$$

$$(v_S^2)_k = \underline{v_S^2} s_k + \overline{v_S^2} \mathbf{1}_{k=0}. \tag{3.23b}$$

From the cusp and sound speeds, again an analytic formula for the Alfvén speed can be found. This is written as

$$v_A^2 = \frac{\overline{v_C^2 v_S^2} + \left(\overline{v_C^2}\underline{v_S^2} + \overline{v_S^2}\underline{v_C^2}\right) \sin\left(\frac{\pi}{l}(r-R)\right) + \underline{v_C^2 v_S^2} \sin^2\left(\frac{\pi}{l}(r-R)\right)}{\left(\underline{v_S^2} - \underline{v_C^2}\right) \sin\left(\frac{\pi}{l}(r-R)\right) + \overline{v_S^2} - \overline{v_C^2}}. \tag{3.24}$$

Unlike the linear case, the denominator in this expression is nowhere zero, so this formula has no poles. Taking derivatives of this expression is clearly not very simple, so as mentioned the Taylor series will be constructed from the Taylor series of its constituent parts. There is a term containing $\sin^2$ in this expression, for which the Taylor series must be first constructed. Similar to the Taylor series for sin, this is written as

$$\sin^2\left(\frac{\pi}{l}(r-R)\right) = \sin^2\left(\frac{\pi}{l}(\zeta + r_c - R)\right) = \sum_{k=0}^{\infty} s_k^2 \zeta^k. \tag{3.25}$$

To avoid confusion in notation, it should be noted that here the coefficients s_k^2 are the coefficients in the Taylor expansion of $\sin^2$ and not the squares of the coefficients s_k. The Taylor series of $\sin^2$ can easily be calculated, yielding formulas for s_k^2:

$$s_0^2 = \sin^2\left(\frac{\pi}{l}(r_c - R)\right), \tag{3.26a}$$

$$s_k^2 = \frac{(-1)^{1+\lceil k/2\rceil}}{2k!}\left(\frac{2\pi}{l}\right)^k \left[\sin\left(\frac{2\pi}{l}(r_c - R)\right)\mathbf{1}_{k\equiv 1 \bmod 2} + \cos\left(\frac{2\pi}{l}(r_c - R)\right)\mathbf{1}_{k\equiv 0 \bmod 2}\right] \qquad \text{if } k \geq 1. \tag{3.26b}$$

With the coefficients of the Taylor series of sin and $\sin^2$ obtained, a formula can be found for the coefficients $(v_A^2)_k$ of the Taylor series for the Alfvén speed. This is done by substituting all Taylor series in equation 3.24 and equating all coefficients of equal degree in ζ left and right, then solving each resulting equation for $(v_A^2)_k$. This way, the coefficients $(v_A^2)_k$ are given according to the recursive formula

$$(v_A^2)_0 = \frac{\overline{v_C^2 v_S^2} + \left(\overline{v_C^2}\,\underline{v_S^2} + \overline{v_S^2}\,\underline{v_C^2}\right) s_0 + \underline{v_C^2 v_S^2} s_0^2}{\left(\underline{v_S^2} - \underline{v_C^2}\right) s_0 + \overline{v_S^2} - \overline{v_C^2}}, \tag{3.27a}$$

$$(v_A^2)_k = \frac{\left(\overline{v_C^2}\,\underline{v_S^2} + \overline{v_S^2}\,\underline{v_C^2}\right) s_k + \underline{v_C^2 v_S^2} s_k^2 - \sum_{j=0}^{k-1}\left(\underline{v_S^2} - \underline{v_C^2}\right) s_{k-j}\,(v_A^2)_j}{\left(\underline{v_S^2} - \underline{v_C^2}\right) s_0 + \overline{v_S^2} - \overline{v_C^2}}. \tag{3.27b}$$

The next parameter to be considered is the square of the magnetic field strength, B^2. The notation introduced so far allows the calculation of B^2 for the sinusoidal profile to be done entirely analogously to the calculation for the linear profile: first the notation

$$W_1 = \frac{1}{\mu}\left(\overline{v_S^2} - \frac{\overline{v_C^2 v_S^2}}{\underline{v_C^2}}\right), \tag{3.28a}$$

$$W_2 = \frac{1}{\mu}\left(\frac{\underline{v_S^2}}{\underline{v_C^2}} - 1 + \frac{\gamma}{2}\right) \tag{3.28b}$$

is introduced, which allows the magnetic field to be written similar to equation 3.12:

$$B^2 = \frac{\gamma P}{W_2}\left(1 - \frac{W_1}{\underline{v_C^2} W_2 \sin\left(\frac{\pi}{l}(r - R)\right) + W_2 + \overline{v_C^2} W_2}\right). \tag{3.29}$$

Either this formula can be used to construct the Taylor series for B^2, or the coefficients can be determined from equation 3.1, now that the coefficients of the sound and Alfvén speed profiles are known. It turns out that both methods are numerically stable. Here,

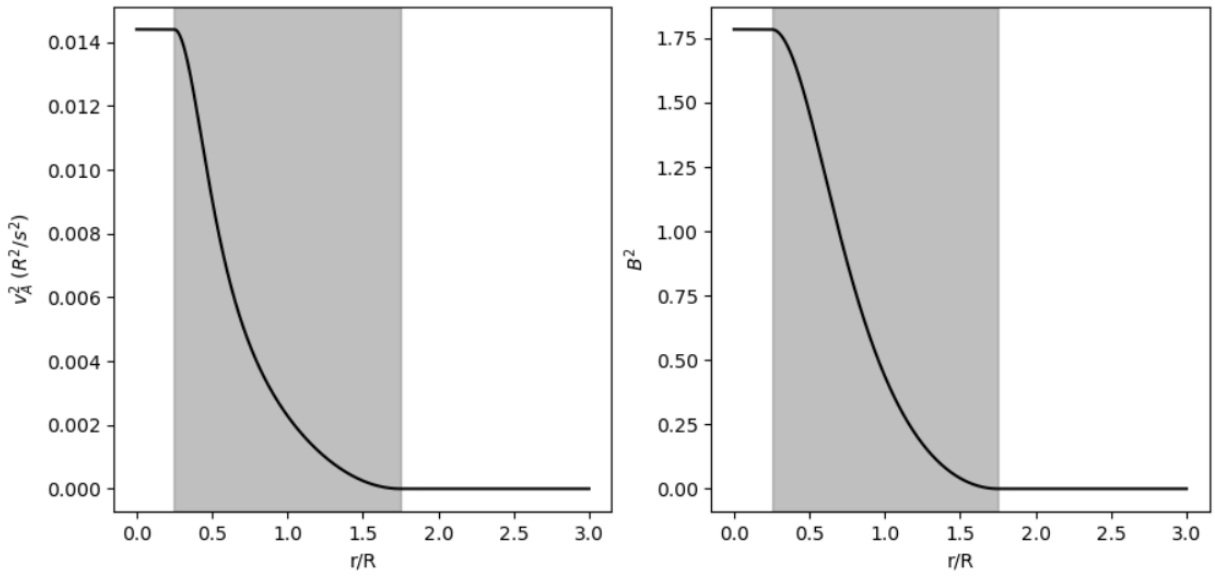

Figure 3.6: Profiles for the squares of the Alfvén speed and magnetic field strength, based on sinusoidal profiles for the squares of cusp and sound speed. $l/R = 1.5$ and all distances are normalised with respect to the cylinder radius R. Values of B^2 are normalised with respect to P.

the coefficients are calculated from those of the sound and Alfvén speeds which yields a more compact form, but a calculation from the analytic formula 3.29 works just as well. Calculating from the coefficients for v_A^2 and v_S^2 yields

$$(B^2)_0 = \frac{\gamma P \left(v_A^2\right)_0}{\frac{\left(v_S^2\right)_0}{\mu} + \frac{\gamma}{2\mu}\left(v_A^2\right)_0}, \tag{3.30a}$$

$$(B^2)_k = \frac{\gamma P \left(v_A^2\right)_k - \sum_{j=0}^{k-1}\left(\frac{\left(v_S^2\right)_{k-j}}{\mu} + \frac{\gamma}{2\mu}\left(v_A^2\right)_{k-j}\right)(B^2)_j}{\frac{\left(v_S^2\right)_0}{\mu} + \frac{\gamma}{2\mu}\left(v_A^2\right)_0}. \tag{3.30b}$$

The profiles of v_A^2 and B^2 are plotted in figure 3.6. They are clearly not pure sine waves like those of v_C^2 and v_S^2 but are still constructed based on periodic functions with their minimum and maximum aligned with the uniform interior and exterior values. From the magnetic field it is again simple to find a formula for the thermal pressure, as they are closely related through the total pressure:

$$p_{\text{th}} = P + \frac{\gamma P}{2\mu W_2}\left(\frac{W_1}{\underline{v_C^2} W_2 \sin\left(\frac{\pi}{l}(r-R)\right) + W_2 + \overline{v_C^2} W_2} - 1\right). \tag{3.31}$$

The coefficients of the power series for p_{th} can also be easily recovered from those of B^2:

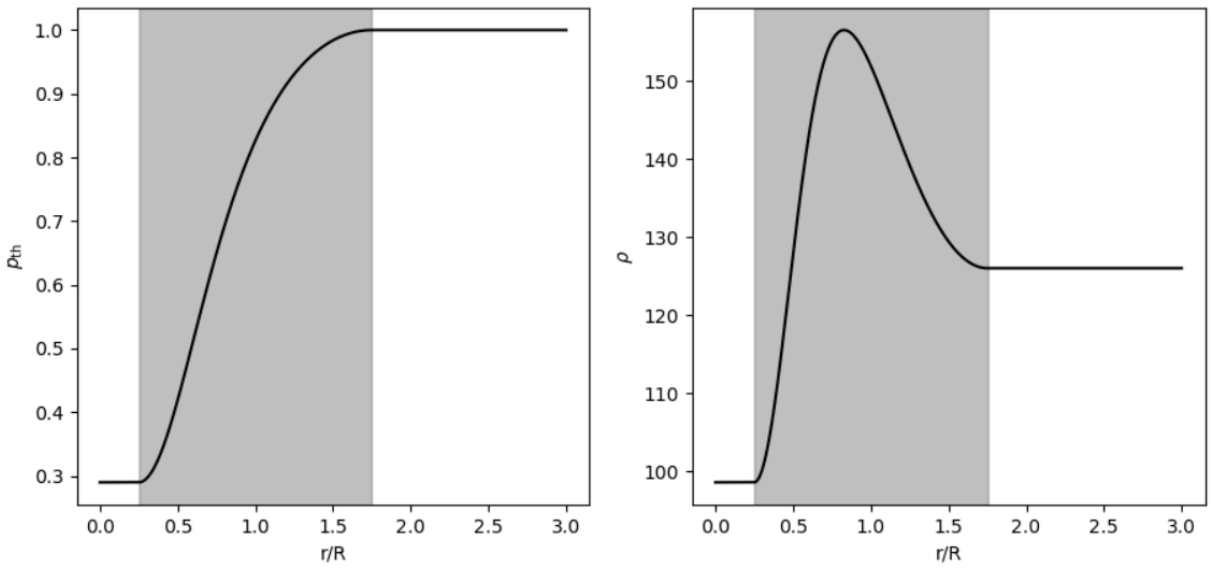

Figure 3.7: Profiles for the thermal pressure and density, based on sinusoidal profiles for the squares of cusp and sound speed. Again, $l/R = 1.5$ and all distances are normalised with respect to cylinder radius R, pressures normalised with respect to P.

$$(p_{\text{th}})_0 = P - \frac{\gamma P\,(v_A^2)_0}{2\,(v_S^2)_0 + \gamma\,(v_A^2)_0}, \tag{3.32a}$$

$$(p_{\text{th}})_k = -\frac{\gamma P\,(v_A^2)_k - \sum_{j=0}^{k-1}\left(\frac{(v_S^2)_{k-j}}{\mu} + \frac{\gamma}{2\mu}\,(v_A^2)_{k-j}\right)(B^2)_j}{2\,(v_S^2)_0 + \gamma\,(v_A^2)_0}. \tag{3.32b}$$

Finally, the profile of the density ρ is considered. Because of the way the notation is introduced, this is again very similar to the linear case. The analytic formula for the density is

$$\rho = \frac{\gamma P}{\mu}\left[\left(\underline{v_S^2} - \underline{v_C^2}\right)\sin\left(\frac{\pi}{l}(r-R)\right) + \overline{v_S^2} - \overline{v_C^2}\right]\left[\underline{v_S^2 v_C^2} W_2 \sin^2\left(\frac{\pi}{l}(r-R)\right)\right.$$
$$\left. + \left(\underline{v_S^2} W_1 + \overline{v_C^2}\,\underline{v_S^2} W_2 + \overline{v_S^2}\,\underline{v_C^2} W_2\right)\sin\left(\frac{\pi}{l}(r-R)\right) + \overline{v_S^2} W_1 + \overline{v_C^2 v_S^2} W_2\right]^{-1}. \tag{3.33}$$

Much like the magnetic field, it will be simpler to construct the coefficients of the Taylor series of ρ directly from the previously obtained coefficients and equation 3.1. This gives a recursive relation for the coefficients $(\rho)_k$, which is

$$(\rho)_0 = \frac{(B^2)_0}{\mu (v_A^2)_0}, \tag{3.34a}$$

$$(\rho)_k = \frac{(B^2)_k - \sum_{j=0}^{k-1} \mu (v_A^2)_{k-j} (\rho)_j}{\mu (v_A^2)_0}. \tag{3.34b}$$

The final two profiles of thermal pressure and density are shown in figure 3.7. Again, the profiles are similar to the linear case but smoother due to the choice of sinusoidal profiles for v_C^2 and v_S^2. This concludes the description of the profiles used in the numerical study. The following sections then deal with the numerical behaviour of the Taylor series of these profiles. First the divergent behaviour is researched, along with the possible causes of this behaviour. The last section then covers a proposition for future research to construct a more numerically valid method for the solution of the dispersion relation.

3.2 Divergence of Taylor series

The Frobenius method explained in chapter 2 assumes that Taylor series expansions of all parameters within the nonuniform boundary layer can be made and that these series converge. However, this section will aim to show that convergent behaviour of the Taylor series in the boundary layer depends on the position of the resonance, meaning that it cannot be guaranteed everywhere. This poses a significant problem: because the coefficients α_k and σ_k in P'_{tr} essentially depend on all parameters, P'_{tr} can only be convergent if all these parameters are convergent as well. If only a solution to the dispersion relation was desired, this problem might be circumvented by using locally convergent solutions, because the dispersion relation 2.33 only depends on the values of P'_{tr} at the edges of the boundary layer. However, a study of the eigenfunctions of P'_{tr} and ξ_r should be conducted as well, for which the entire boundary layer is relevant. Hence a study of the slow resonance is impossible if no convergent profiles for the plasma parameters can be found.

Because the profiles for the parameters are defined consecutively, once divergent behaviour occurs in one profile, it will also occur in all subsequent profiles. For example, by choosing the profiles of v_C^2 and v_S^2 as default profiles, the profile for v_A^2 will become divergent and as a result those of B^2, ρ and p_{th} will be too. Changing the choice of default profiles will also change the order in which the four derived profiles are constructed and this will not remove the divergent behaviour, which will simply emerge in a different profile. For example, choosing v_C^2 and v_A^2 as default profiles makes the profile for v_A^2 convergent, but also causes the profile for v_S^2 to diverge. The same reasoning can be made for B^2, ρ and p_{th} as well. Hence the choice of default problems can be made arbitrarily. As mentioned before, here the profiles of v_C^2 and v_S^2 will always be chosen as default profiles. As a result, the profile of v_A^2 will be the first to diverge. Because of this, the study of the divergent behaviour will be made regarding the profile of v_A^2.

For the linear profile, it is analytically clear that the convergence radius of the Taylor series of v_A^2 is limited, due to the presence of the pole. As an illustration, figure 3.8 shows the rational function that is used in the transitional region, this time continued in the entire domain. Of course, negative values of v_A^2 and r have no physical meaning here, this function can only be considered physical within the shaded region. As calculated before, for a value of $l/R = 1.5$ the pole is situated at $r = 0.09R$ and the boundary layer spans the region of $[0.25R, 1.75R]$. As is known for rational functions, the size of the convergence radius is then determined by the distance between the pole and the center of the expansion. For iterations where the resonance position is situated sufficiently close to the interior edge of the boundary layer, this convergence radius will then be smaller than the boundary layer, resulting in divergent behaviour towards the outer edge of this layer. For example, if the resonant position were to be taken at $r = 0.5R$, the distance to

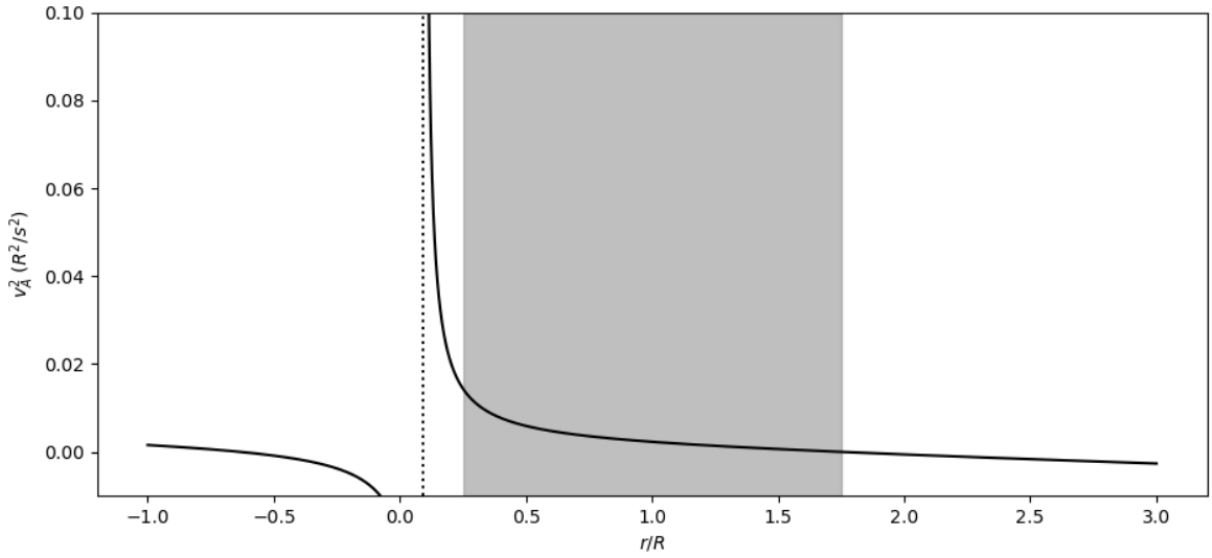

Figure 3.8: Plot of the profile used for v_A^2 as based on linear profiles for v_C^2 and v_S^2, continued in the uniform regions. For illustrative purposes, the domain is extended to include negative values of r which of course has no physical interpretation. Within the shaded region this function is exactly equal to v_A^2, outside uniform values are imposed for v_A^2. The position of the pole is plotted as a dashed line.

the pole is $0.41R$ and convergence would only be expected in the region of $[0.09R, 0.91R]$ which clearly does not cover the boundary layer. Overall, because the pole is so close to the inner edge of the boundary layer, convergence within the entire boundary layer can only really be expected when the resonance position is assumed to be beyond $r = 0.92R$. At $r = 0.92R$ the pole is equally distant from the resonant position as the outer edge of the boundary layer, meaning that this is the most inward position for which there is convergence in the entire boundary layer.

It should be noted that this divergence does not depend on the thickness of the boundary layer. This is again most easily seen when looking at the pole of v_A^2 in the linear profile. This pole arises due to the term $v_S^2 - v_C^2$ in the denominator of v_A^2, as seen in equation 3.2. Because here v_S^2 and v_C^2 are linear functions with different slopes, they will always intersect. When taking values for these parameters typical for magnetic pore conditions, this intersection lies close to the inner edge of the boundary layer. If the thickness of the boundary layer changes, the slopes of these linear functions change accordingly, in such a way that the distance between the pole and the boundary layer does not change relative to the thickness of this boundary layer, meaning that the same fraction of this layer will have divergent behaviour, regardless of the value of l/R.

The effect of the pole on the convergence radius is shown in figure 3.9. This figure shows the Taylor series approximation together with the analytic profile for v_A^2 for varying positions of the resonance. It is clear from this figure that the interval of convergence increases as r_c moves away from the pole and that r_c is always in the middle of this interval. The bottom plot shows the limiting case of $r_c = 0.92R$, where indeed the Taylor series is a good approximation of the function in a region that just covers the boundary layer. It is clear from this figure that the resonance position must be at least as far as $0.92R$ to guarantee convergent behaviour within the boundary layer. In order to generalise this value of r_c to arbitrary thickness l, it is easier to instead use a dimensionless parameter

$\theta_c \in [0, 1]$ defined through

$$r_c = R - \frac{l}{2} + \theta_c l. \tag{3.35}$$

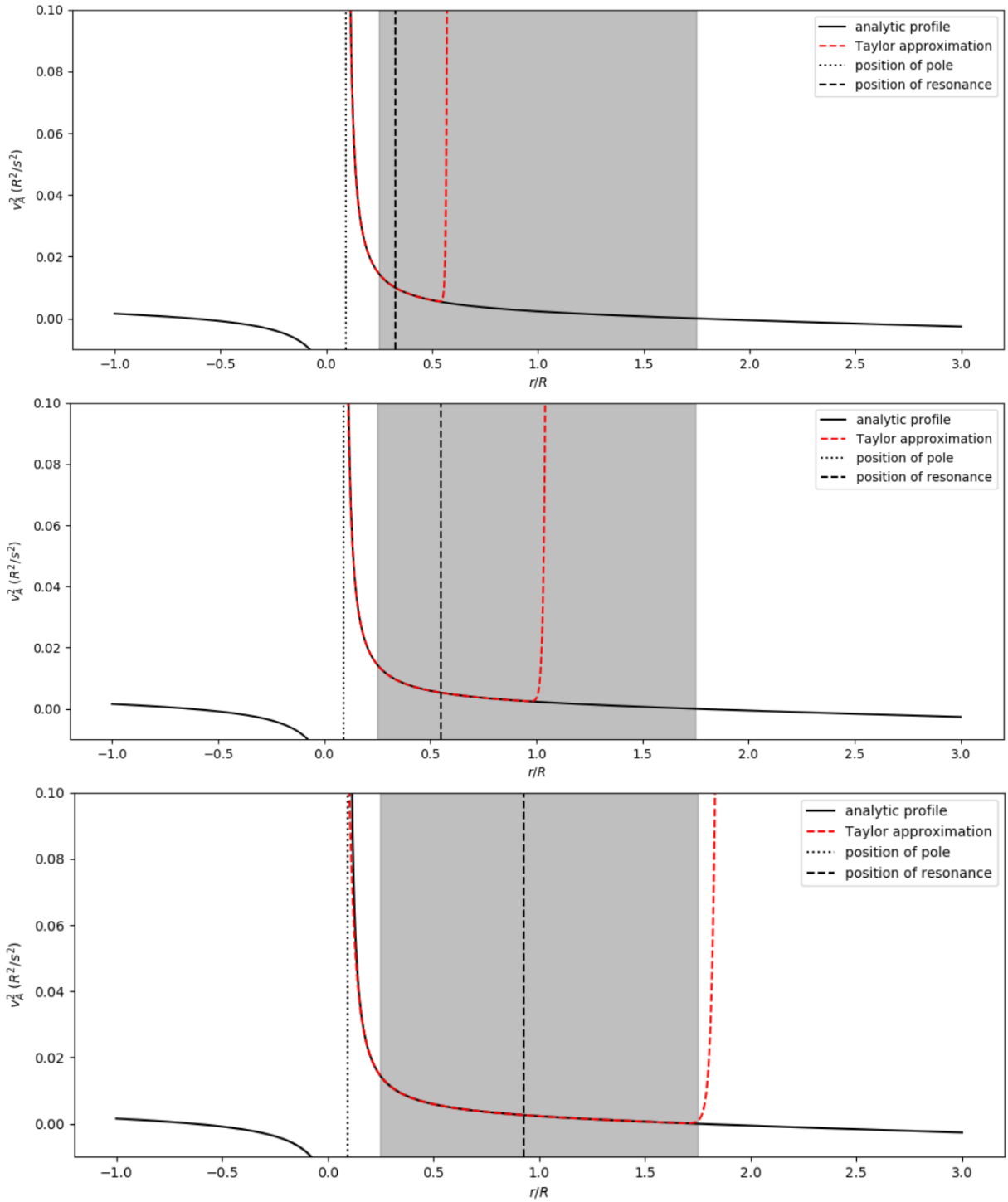

Figure 3.9: Comparison of the Taylor approximation for v_A^2 in the linear case depending on varying positions of the resonance position. From top to bottom: $\theta_c = 0.05$ ($r_c = 0.325R$), $\theta_c = 0.2$ ($r_c = 0.55R$), $\theta_c = 0.447$ ($r_c = 0.92R$). All values are taken for thickness $l/R = 1.5$.

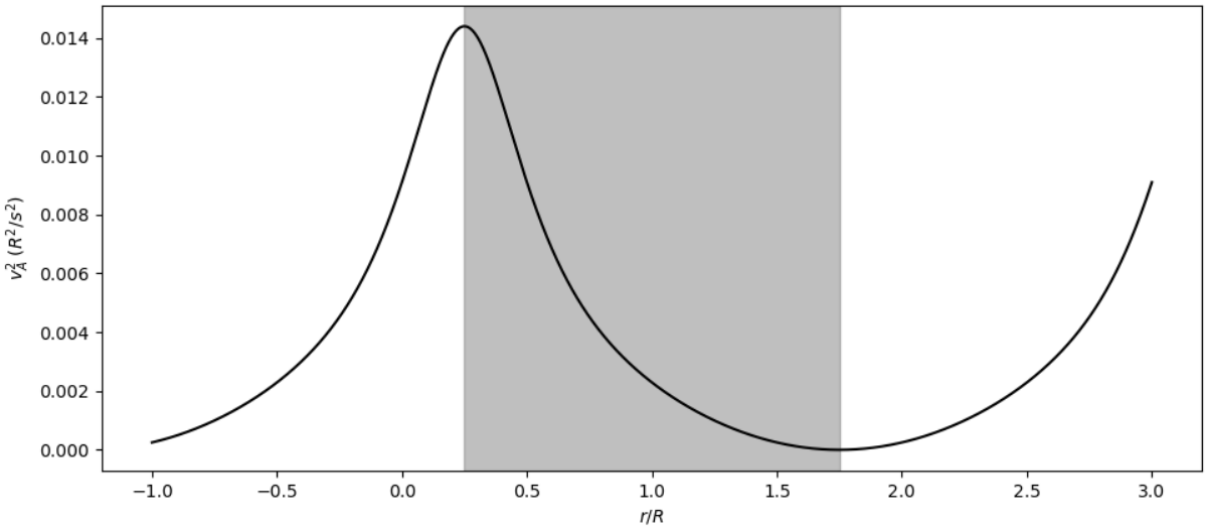

Figure 3.10: Plot of the profile used for v_A^2 as based on sinusoidal profiles for v_C^2 and v_S^2, continued in the uniform regions. For illustrative purposes, the domain is extended to include negative values of r which again has no physical interpretation. Within the shaded region this function is exactly equal to v_A^2, outside uniform values are imposed for v_A^2.

θ_c is then the relative position of r_c within the boundary layer. $\theta_c = 0$ corresponds to the inner edge of the boundary layer, $\theta_c = 1$ to the outer edge. Using this parameter instead, the critical position of $r_c = 0.92R$ is found for $\theta_c = 0.447$ which now holds for arbitrary thickness l.

The linear case clearly gives rise to divergent behaviour due to the presence of a pole. It could then be argued that this problem might be solved by instead of considering a Taylor series expansion, a Laurent series expansion could be be considered, which includes an extra term to deal with the pole. After all, this is how the treatment of $k_\perp^2$ was done. However, it should be noted that $k_\perp^2$ has a pole at $\zeta = 0$, which is the expansion point. The pole for v_A^2 instead lies somewhere else than the expansion point, so considering this would mean performing an expansion at another point than $\zeta = 0$. While this idea is not a priori wrong and changing the center of expansion is to some extent possible, in the final section of this chapter it is shown that this may not be the best solution.

Next, the sinusoidal profile is considered. Again, the study of the divergence of the Taylor series is done by studying the profile for the square of the Alfvén speed. This profile is plotted in figure 3.10, where again the profile is continued in the uniform regions for illustrative purposes. Again, the domain is extended to include negative values of r which do not have any physical meaning. This profile, which is now periodic with a period of $2l$, does not contain a pole, unlike the linear one. Similarly, the profiles of ρ, B^2 and p_{th} will also not contain a pole.

Although there is now no pole, it seems that the wave top at the inner edge of the boundary layer now causes the convergence radius to be limited, as can be seen in figure 3.11. Similar to the pole in the linear profile, the closer the resonance position is taken to this top the smaller the convergence domain. Because the function is now still well-defined in the vicinity of this top, it can still be locally approximated by the Taylor series, albeit with a smaller convergence radius. As the resonance position moves away from the inner edge of the boundary layer, the region where the Taylor series is convergent moves along

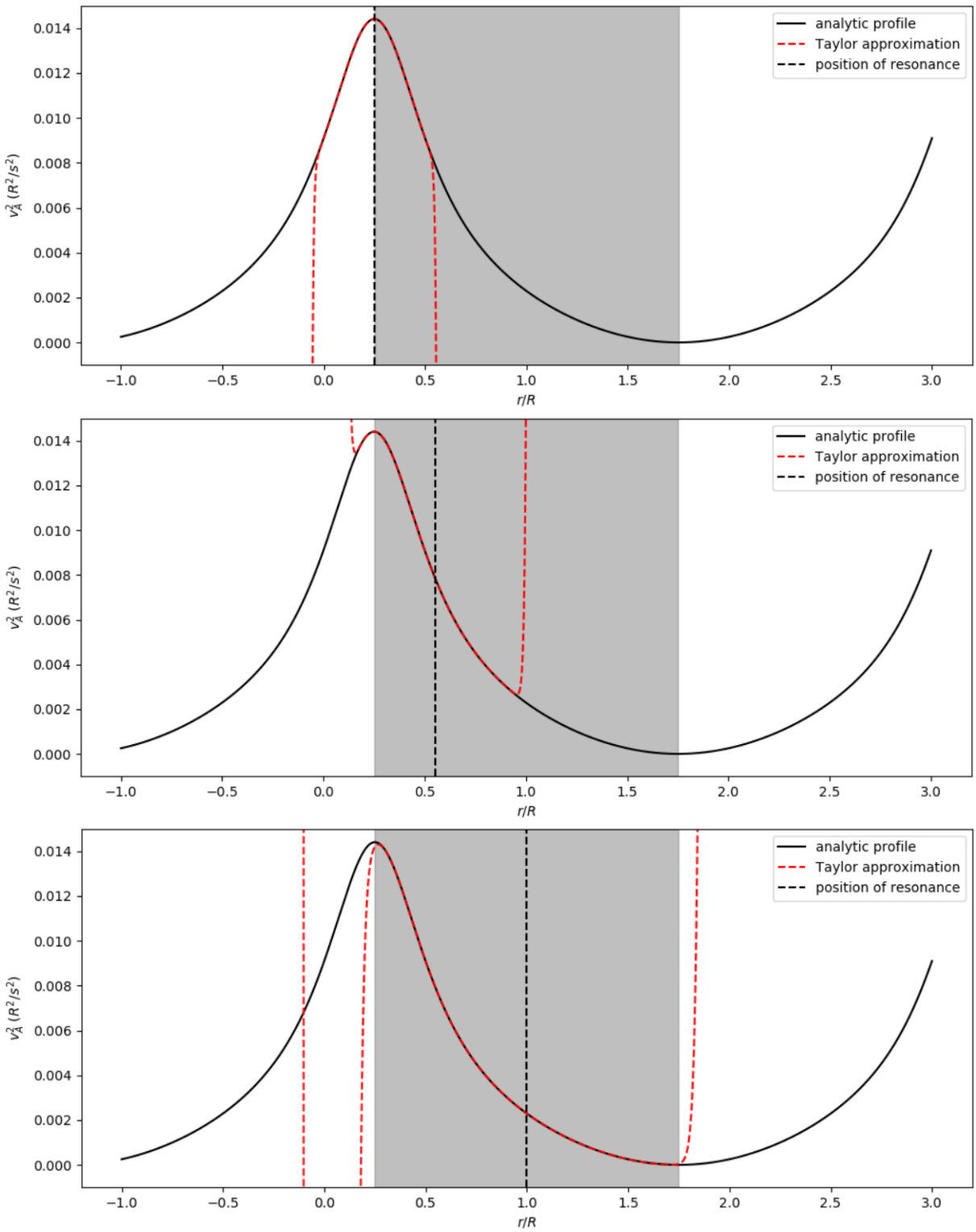

Figure 3.11: Comparison of the Taylor approximation for v_A^2 in the sinusoidal case depending on varying positions of the resonance position. From top to bottom: $\theta_c = 0$, $\theta_c = 0.2$, $\theta_c = 0.5$. All plots are made for thickness $l/R = 1.5$.

with it and increases.

If this series of plots were continued, the largest convergence radius would be obtained

at $\theta_c = 1$, for which an entire period is well approximated and divergence would occur at the wave tops situated at $\theta_c = 0$ and (hypothetically) $\theta_c = 2$. Because this top by construction lies precisely at the inner edge of the boundary layer, the critical value for which convergence is reached within the entirety of this layer occurs now for $\theta_c = 0.5$, which coincides with $r_c = R$ for all values of l. For larger values of θ_c there will always be divergence at the inner edge of the boundary layer as in the bottom plot of figure 3.11, which is just far enough to approximate the profile within the entire boundary layer.

The cause of the divergence in the sinusoidal case is less straightforward to pinpoint than the linear case, because now the profile and all its derivatives are well-defined throughout the domain. Because the profile is bounded and everywhere differentiable, the cause of the divergence presumably lies in the higher-order derivatives which may have very large values at the inner edge of the boundary layer. Either way, the convergence radius of the Taylor series is always limited even though for some values of θ_c it is large enough to cover the entire boundary layer. This convergence radius is largely independent of $k_{\max}$. In figure 3.11 $k_{\max} = 50$ is chosen, but a higher value of $k_{\max}$ will still give similar results, there will always be divergent behaviour and the critical value of θ_c does not depend on the chosen value for $k_{\max}$. The code used to calculate the Taylor series is accurate up to $k_{\max} \approx 120$. For higher values, overflow occurs and the calculation is no longer possible.

The problem of divergent behaviour is unique to the study of plasmas where $\beta \approx 1$. For example, in the study performed by Soler et al. (2013) for the Alfvén resonance, this problem did not occur. This is because in the coronal regimes they study $\beta \ll 1$ which means that the approximation of $v_S = v_C = 0$ is valid. In this limit the magnetic field strength is constant everywhere and the entire system can be described through a variation of only density. Then the profile for ρ is the only profile that occurs, so bad behaviour of derived profiles will not happen because there are no derived profiles, only the profile of ρ which can be specified upfront.

The final section of this chapter will propose several solutions to this problem of divergence. However, none of these solutions are fully developed and a solution for the dispersion relation will not be reached. Future research will then have to consider and implement these solutions, to hopefully arrive at a more stable method which can solve the dispersion relation 2.33 and study the eigenfunctions and damping rate of the slow surface mode.

3.3 Possible solutions to the divergence problem

3.3.1 Change of expansion point

The Frobenius method consists of expanding P'_{tr} at the singular point $\zeta = 0$. As can be seen on figures 3.9 and 3.11, the position of this singular point can pose problems when constructing Taylor series expansion of the constituent parameters of P'_{tr}. However, there is no requirement that the Taylor series of these parameters are themselves expanded at $\zeta = 0$. A possible solution could then consist of expanding the parameters at a different position ζ_0, such that the Taylor series are convergent in the entire boundary layer. As investigated before, an example of such a position would be $\zeta = R - r_c$, which corresponds to $\theta_c = 0.5$. For both the linear and sinusoidal cases this yields convergent behaviour

within the entire boundary layer. Some additional calculations are then needed to make a general expansion point for the plasma parameters compatible with the expansion of P'_{tr} which is always performed at $\zeta = 0$.

Changing the coefficients of the Taylor series considered earlier in this chapter to allow expansion at an arbitrary point ζ_0 is not too difficult to do. For the linear case, the coefficients were obtained by explicitly calculating a general form of the k-th derivative of the profile, from which the Taylor series is easily constructed. Changing from an expansion at $\zeta = 0$ to one at $\zeta = \zeta_0$ then simply means evaluating this derivative at $r = r_c + \zeta_0$ instead of evaluating it at $r = r_c$. This yields a Taylor series in $(\zeta - \zeta_0)$ instead of in ζ without much extra effort. For the sinusoidal case, all profiles were derived from the profiles of sin and $\sin^2$. In this case it then suffices to adapt the coefficients of the Taylor series for these two functions. Profiles for all parameters then follow from these two using the same formulas as before. Generalising the coefficients s_k and s_k^2 for these sinusoidal profiles is very straightforward and yields

$$s_k = \frac{(-1)^{\lfloor k/2 \rfloor}}{k!} \left(\frac{\pi}{l}\right)^k \left[\sin\left(\frac{\pi}{l}(\zeta_0 + r_c - R)\right) \mathbf{1}_{k\equiv 0 \bmod 2} + \cos\left(\frac{\pi}{l}(\zeta_0 + r_c - R)\right) \mathbf{1}_{k\equiv 1 \bmod 2}\right], \tag{3.36}$$

and

$$s_0^2 = \sin^2\left(\frac{\pi}{l}(\zeta_0 + r_c - R)\right), \tag{3.37a}$$

$$s_k^2 = \frac{(-1)^{1+\lceil k/2 \rceil}}{2k!} \left(\frac{2\pi}{l}\right)^k \left[\sin\left(\frac{2\pi}{l}(\zeta_0 + r_c - R)\right) \mathbf{1}_{k\equiv 1 \bmod 2} + \cos\left(\frac{2\pi}{l}(\zeta_0 + r_c - R)\right) \mathbf{1}_{k\equiv 0 \bmod 2}\right] \qquad \text{if } k \geq 1. \tag{3.37b}$$

These also yield Taylor series in $(\zeta - \zeta_0)$. It can be seen that if the center of the boundary layer $r = R$ is chosen as expansion point, then $\zeta_0 = R - r_c$ and all sines and cosines in these expressions become 0 and 1, respectively. These new, more general profiles can then be used to find a profile for P'_{tr} which is convergent everywhere. However, this still requires the expressions for h, p and q in chapter 2 to be adapted to these profiles as well, since those profiles currently assume that the power series of the parameters are expressed as series in ζ. With such new expressions for h, p and q the same calculations can be made as were done in chapter 2 to arrive at slightly altered expressions for α_k and σ_k in the formula for P'_{tr}.

In order to freely change the expansion point, a conversion formula is needed, to allow coefficients to be changed from any expansion point ζ_0 to any other expansion point ζ'_0. Given two such series

$$\sum_{k=0}^{\infty} f_k(\zeta - \zeta_0)^k \qquad \text{and} \qquad \sum_{k=0}^{\infty} g_k(\zeta - \zeta'_0)^k, \tag{3.38}$$

the coefficients f_k and g_k can be related by the formula

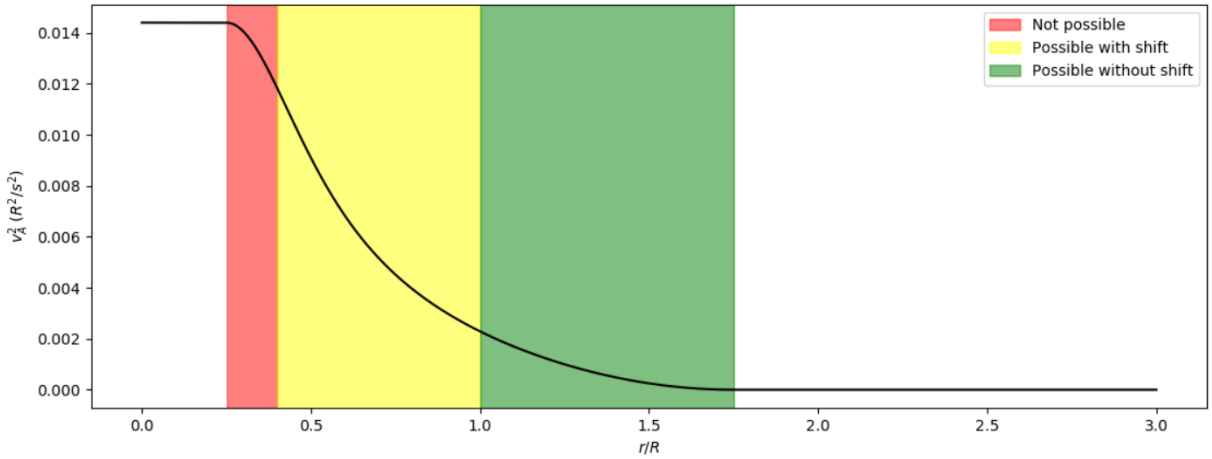

Figure 3.12: Plot of the Alfvén speed in the sinusoidal case, with the boundary layer divided in regions based on the accuracy of equation 3.39. Initial $k_{\max} = 100$, colours show where a final accuracy of 20 degrees is attainable.

$$f_k = \sum_{j=k}^{\infty} g_j \binom{j}{k} (\zeta_0 - \zeta_0')^{j-k}. \tag{3.39}$$

Using for example $\zeta_0 = 0$ and $\zeta_0' = R - r_c$ or vice versa gives the conversion formula for the specific case mentioned before. An important remark with this formula should be made regarding its accuracy. Equation 3.39 itself is exact, but can of course not be implemented exactly due to the infinite sum in the expression. As is done with all other series, when numerically implemented a sufficiently large truncation number $k_{\max}$ is chosen. Then all infinite sums are truncated at $k_{\max}$. However, unlike the series used so far, this sum only starts at k when considering the coefficient f_k. This means that if the conversion is attempted for a number k which is close to $k_{\max}$, this will not give an accurate result, especially if the convergence of the coefficients is slow. Hence this formula limits the maximal accuracy that can be obtained. This limit can be pushed further by considering a greater value of $k_{\max}$ prior to the shift to retain a few extra degrees of accuracy, but this happens at a significant computational cost. Furthermore, the distance between ζ_0 and ζ_0' also limits the accuracy of this formula, since for greater distances this sum will converge more slowly meaning that more accuracy is lost due to the truncation.

Figure 3.12 illustrates the loss of accuracy of equation 3.39 in the case of a sinusoidal profile. It is assumed here that an expansion is performed at $\zeta_0 = R - r_c$ and with a truncation number $k_{\max} = 100$. This time, the boundary layer is coloured according to the loss of accuracy of equation 3.39 when this formula is used to convert from an expansion at ζ_0 to an expansion around the resonance point itself. If the resonance point lies in the green region, then the profile for the Alfvén speed is always convergent as has been shown before. Hence a conversion is not necessary, and calculations can simply be made with an expansion at $\zeta = 0$. Within the yellow region, the expansion at $\zeta = 0$ will be divergent within the boundary layer, so this conversion is necessary. The maximum value of k for which equation 3.39 yields accurate values decreases as the resonance position moves to the left, but within the yellow region it is still acceptable (a maximum value for k of at least 20). Within the red region, the loss of accuracy is too great and even an

initial $k_{\max}$ of 100 will result in a final accuracy of less than 20 degrees. Using a smaller value of $k_{\max}$ will increase the size of the red region. A larger value of $k_{\max}$ should decrease the size of this region, but a value significantly larger than 100 is in practice unrealistic since this will cause overflow.

With this proposed method of shifting the expansion point it should be possible to find convergent results for about 90% of iterations of the resonance point as shown in figure 3.12. Hence a priori it is very likely that within this region a solution to the dispersion relation can be found and the eigenfunctions of P'_{tr} and ξ_r can be studied. However, as illustrated by figure 2.1, the phase speed of the slow surface mode lies very closely to the internal cusp speed for the magnetic pore conditions. Hence it is likely that the resonance position actually lies close to the inner edge of the boundary layer, which is precisely where the red region is situated. It might be possible that this position lies close to the yellow region so the shift method might yield acceptable results. Furthermore, for the linear case the red region is smaller as the optimal position to perform the expansion is found at $\theta_c = 0.447$ which lies somewhat closer to the inner edge than the optimal position $\theta_c = 0.5$ of the sinusoidal case. However, it is not guaranteed that this shift method will yield satisfactory results, as even then the resonance position might be too close to the inner edge. Some other methods may be better suited to deal with this.

3.3.2 Different parameter profiles

Changing the expansion point may or may not yield desirable results, but maybe an entirely different and simpler approach could bring more insight. So far, only linear and sinusoidal profiles have been considered. While these are certainly the simplest and most commonly researched profiles, in theory any profile which guarantees continuity within the domain can be chosen. Here, two other candidate profiles are shown, which may give better results than the linear and sinusoidal profiles. These two candidate profiles are the parabolic profile, and the hyperbolic tangent profile.

The parabolic profile is a very simple alteration of the linear profile. For the square of the cusp speed this profile takes on the form

$$v_C^2 = v_{Ci}^2 - \frac{v_{Ci}^2 - v_{Ce}^2}{l^2}\left(r - R + \frac{l}{2}\right)^2 . \tag{3.40}$$

Removing the square of the term in brackets and writing l instead of l^2 yields the linear profile that has been used before. Instead of a linear connection of the internal and external parameters, this now gives a parabolic shape of the profile, in such a way that the top of the parabola is situated at the inner edge of the boundary layer. For the sound speed, an equivalent profile is then again considered. The other four parameters can again be derived from these two, but these profiles are not given here. The left plot in figure 3.13 shows the parabolic profile.

Like the linear profile, the parabolic profile is not everywhere differentiable and will result in poles for the other profiles. However, the position of these poles may be significantly different this time. If the poles are further away from the edge of the boundary layer, the convergence radius will be larger, leading to convergent behaviour for more iterations. Furthermore, this profile has most of the variation of the cusp speed situated towards

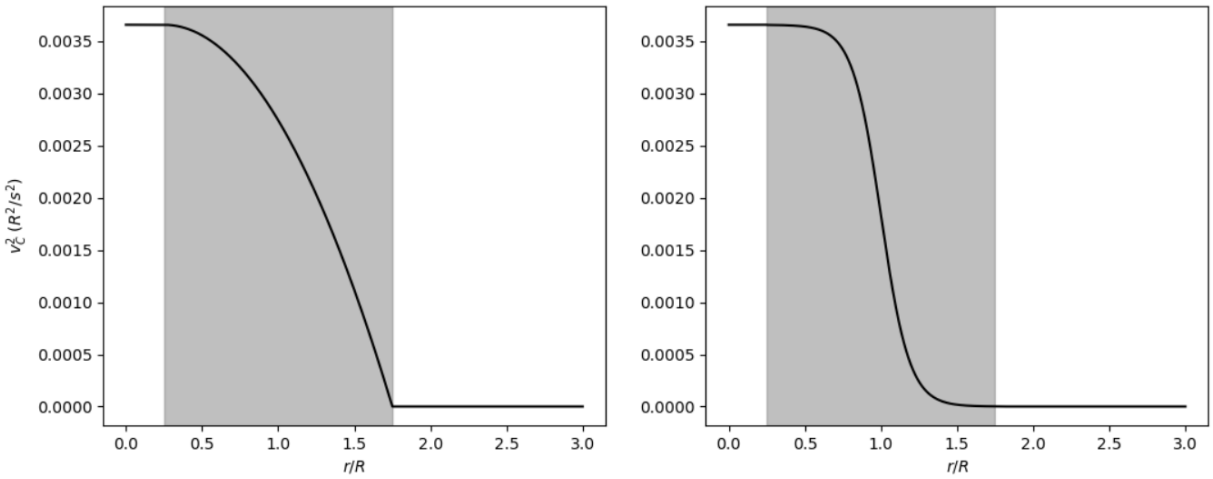

Figure 3.13: Parabolic and hyperbolic tangent profiles for the square of the cusp speed. The scaling factor for the hyperbolic tangent profile is $\mathcal{F} = 8/l$.

the outer edge of the boundary layer. This will result in the resonance position moving outward, further into the region where convergent behaviour is more likely. This is specifically interesting if this profile were coupled with the shift method, because for this profile it is more likely that the resonance position will be somewhere the loss of accuracy in equation 3.39 is still acceptable. These claims have not yet been investigated, but the parabolic profile may give a possible solution.

A second candidate profile is the hyperbolic tangent profile shown in the right plot of figure 3.13. This profile takes on the form

$$v_C^2 = v_{Ci}^2 + \left(v_{Ce}^2 - v_{Ci}^2\right)\left(\frac{1 + \tanh\left(\mathcal{S}(r - R)\right)}{2}\right), \tag{3.41}$$

where $\mathcal{S}$ is a scaling factor that depends on the steepness of the profile. To guarantee continuity (in a numerical sense), $\mathcal{S}$ needs to be larger than some threshold value. This is because $\tanh(x)$ only goes to ± 1 in the limit for $x \to \pm\infty$, hence this limiting behaviour must be sufficiently captured. A value of $\mathcal{S} = 8/l$ appears to be sufficient for this threshold. Larger values may be considered, but these will lead to a steeper profile, which is essentially equivalent to assuming a lower value of l/R. Similar to before, the sound speed will follow an equivalent profile and the other parameters can be derived from those of the cusp and sound speeds, but these profiles are not given here. The hyperbolic tangent profile has a similar advantage as the parabolic profile, where most of the variation is situated in the center of the boundary layer. This again has the effect of pushing the resonance position outwards, into a region where convergence of the Taylor series is more likely. The hyperbolic tangent profile may also result in derived profiles that are better behaved than those derived from the sinusoidal profile, but this claim has not been investigated.

The problem of divergent behaviour might simply be a problem confined to the linear and sinusoidal profiles. If this were the case, a smart choice of profile would be a very simple way to fix all problems encountered in this chapter. However, this claim requires further investigation since the profiles of Alfvén speed, magnetic field, density and thermal

pressure are obtained in a nontrivial way from the initial profiles. This makes their behaviour, and especially the behaviour of their Taylor series difficult to predict. After all, the Taylor series of a simple sinusoidal profile are very well-behaved, but these already give rise to divergent behaviour. The same may easily be true for these two suggested profiles.

The two options proposed thus far are not mutually exclusive: it could, for example, be possible to consider a parabolic profile where convergent behaviour is obtained in some regions only by considering a change in expansion point. It seems that in any case the parabolic and hyperbolic tangent profiles are better suited for a combination with the shift method than the linear or sinusoidal profiles, because they have little variation of the cusp speed near the inner edge of the boundary layer. This pushes the resonance point, which is close to this inner edge for the linear and sinusoidal profiles, more to the center of the boundary layer where convergent behaviour is more likely.

A drawback of this proposed solution, were it to work, is that this limits the study to a specific profile. In general it is desirable that the method should work for an arbitrary profile. As shown by Soler et al. (2014), the chosen profile for the parameters in the boundary layer significantly affects the frequency obtained with the method. If either the parabolic or the hyperbolic tangent profile yields solutions, then these solutions are only valid for this specific profile and more general solutions cannot be obtained. In the last section then, an entirely different possible solution is proposed which allows for any profile to be considered.

3.3.3 Complex frequencies

An important goal of studying the resonance of waves in solar structures is to study the effect of resonant damping. Resonant damping occurs when the solution frequency of the dispersion relation has a negative imaginary part. So far, however, the frequency ω has always been studied as a real frequency in the real interval $[\omega_{Ce}, \omega_{Ci}]$. This may seem strange, especially since the study of the dispersion relation in the TB assumption showed explicitly that the dispersion relation then contains an imaginary part. This imaginary part also shows up in the full dispersion relation 2.33, specifically in the logarithmic term of P_2' for negative values of ζ. This term is present in the expressions $\mathcal{F}_i$ and Γ_i. The study of ω as a real frequency throughout chapters 2 and 3 is a deliberate choice, where only the real part of the dispersion relation is considered. The idea is to first consider the solution for the real part and then searching for the corresponding imaginary part of the frequency. This makes the search algorithm considerably faster, since it involves a one-dimensional grid as search domain instead of a two-dimensional one. Because the divergence problem made it impossible to find the real solution, the search for the imaginary part was never started. Within this work, priority was given to first solve the problem for the real part, after which the imaginary part could be solved. Unfortunately this solution, as shown extensively before, was not reached.

A different approach would then be to consider the frequency as a complex quantity from the start and solving the dispersion relation in its entirety. This does not change the divergent properties of the quantities themselves, but might have the effect of placing the resonance position somewhere in the complex plane where the series expansions are better behaved. It is unlikely that this method in itself solves the problem, since in general the

imaginary part is considerably smaller than the real part (see e.g. Yu et al. 2017a). Hence the inclusion of the imaginary part may only have a small effect on the position of the resonance, which will likely remain somewhere the series expansions are divergent. However, this method can be combined with the shift method or with other profiles. This combination may yield a solution if the inclusion of the imaginary part is insufficient in itself.

As mentioned, none of these three proposed solutions are mutually exclusive. It is possible that one of them may be sufficient to find a solution to the dispersion relation. If none of them are sufficient by themselves, perhaps a combination of two or even all three may yield a solution. It is unclear to what extent a combination of these propositions improves the behaviour. It may only be a very marginal improvement, or they may yield much better results when combined. Everything proposed in this last section consists of claims that have not been fully explored, so it will be up to future research to investigate them further. It is also not guaranteed that a solution can be reached with any of these propositions. Again, future research may yield entirely new methods which may be better suited than any of the proposals mentioned in this section.

Conclusion

The study of the slow resonance performed in this thesis consisted of two main parts: an analytical derivation of the dispersion relation and a numerical study of this relation. Overall the analytical calculations yielded results that were consistent with previous research. The numerical part on the other hand, gave complications which led to a study of the numerical behaviour of the profiles considered and several proposals that may give a solution in future research.

The method used to find a dispersion relation was based on previous work performed by Soler et al. (2013). This method consists of solving the equations that describe the system explicitly within the interior and exterior layers of the cylinder, which are assumed to be uniform. In the nonuniform boundary layer, these equations cannot be easily solved, so a Frobenius expansion is considered at the resonance point. The coefficients of this expansion can be found by considering power series for the three characteristic plasma speeds, as well as the magnetic field, density and thermal pressure. By connecting the solutions in the uniform layers to those in the nonuniform layer the dispersion relation can then be found.

Previous results often assumed that the thickness of the boundary layer is much smaller than its radius, the so-called TB assumption. The method considered here is a more general approach which yields results that are valid for arbitrary thickness of the boundary layer. The TB case was then studied as a limiting case of the general solution. As expected, in this limit the results by Yu et al. (2017a), who studied the slow resonance for magnetic pores in the TB limit, were recovered. This confirms the usefulness of the method, which now yields more general results.

The numerical implementation of these results proved to be more difficult. Complications arose in the form of divergence of the Taylor series for several parameters. Such complications are unique to the study of the slow modes. For example, in the study of the Alfvén resonance done by Soler et al. (2013) these did not occur because for the Alfvén resonance, the $\beta = 0$ approximation is valid which makes the profile for the density the only relevant profile. For the slow resonance, profiles of six different parameters occur in the expressions. Because all these profiles must be consistent with each other, some profiles are less well-behaved.

Two profiles were studied in detail: a linear and sinusoidal profile. These both showed the divergence, albeit in a different way. For the linear profile, the cause clearly lies with a pole for the derived profile of the Alfvén speed. The sinusoidal profile on the other hand does not contain poles but has different behaviour that also leads to a shape that cannot be accurately approximated by a Taylor series.

Finally, three possible solutions were proposed. First the possibility of constructing Taylor series of the profiles at a different point was considered, which allows for the expansion

point to be chosen in such a way that the profile is convergent. For both the linear and sinusoidal profiles, the center of the boundary layer is a good choice for such a point. Another possible solution may be as simple as changing the profile. Here the parabolic and the hyperbolic tangent profiles were proposed, but perhaps an even different profile yields better results. The last proposed solution is to include the imaginary part of the frequency already at the start of the calculations. This may also make it easier to find a solution to the dispersion relation.

All three proposed solutions are no more than proposals. It will be up to future research to investigate the validity of these claims or maybe propose new options. Regardless of what method is used, if the dispersion relation can be solved, the further implementation of the method is very straightforward. Once this problem of divergence is solved, it will be possible to perform a study of the eigenfunctions and the damping rate due to the slow resonance.

Bibliography

[1] Aschwanden, M., *Physics of the solar corona: An introduction with problems and solutions*, Springer, 2005

[2] Dorotovič, I., Erdélyi, R., Karlovský, V. 2008, IAU Symp., 247, 351

[3] Edwin, P., Roberts, M. 1982, Sol. Phys., 76, 239

[4] Edwin, P., Roberts, M. 1983, Sol. Phys., 88, 179

[5] Goossens, M., Hollweg, J., Sakurai, T. 1992, Sol. Phys., 138, 233

[6] Goossens, M., Van Doorsselaere, T., Soler, R., Verth, G. 2013, ApJ, 768, 191

[7] Grant, S., Jess, D., Moreels, M., Morton, R., Christian, D., Giagkiozis, I., Verth, G., Fedun, V., Keys, P., Van Doorsselaere, T., Erdélyi, R. 2015, ApJ, 806, 132

[8] Keys, P., Morton, R., Jess, D., Verth, G., Grant, S., Mathioudakis, M., Mackay, D., Doyle, J., Christian, D., Keenan, F., Erdélyi, R. 2018, ApJ, 857, 28

[9] Krishna Prasad, S., Banerjee, D., Van Doorsselaere, T. 2014, ApJ, 789, 118

[10] Mandal, S., Magyar, N., Yuan, D., Van Doorsselaere, T., Banerjee, D. 2016, ApJ, 820, 13

[11] Nakariakov, V., Pilipenko, V., Heilig, B., Jelínek, P., Karlický, M., Klimushkin, D., Kolotkov, D., Lee, D., Nisticò, G., Van Doorsselaere, T., Verth, G., Zimovets, I. 2006, Space Sci. Rev., 200, 75

[12] Soler, R., Oliver, R., Ballester, J., Goossens, M. 2009 ApJL, 695, L166

[13] Soler, R., Goossens, M., Terradas, J., Oliver, R. 2013, ApJ, 777, 158

[14] Soler, R., Goossens, M., Terradas, J., Oliver, R. 2014, ApJ, 781, 111

[15] Van Doorsselaere, T., Andries, J., Poedts, S., Goossens, M. 2004, ApJ, 606, 1223

[16] Yu, D., Van Doorsselaere, T., Goossens, M. 2017, A&A, 602, A108

[17] Yu, D., Van Doorsselaere, T., Goossens, M. 2017, ApJ, 850, 44

Appendix A

Expressions of expansion coefficients

$$\alpha_0 = 1 \tag{A.1}$$

$$\alpha_1 = -\frac{r_c f_0 - r_c^2 f_1 + r_c^2 f_0 \kappa_{-1}}{2 r_c^2 f_0} \alpha_0 \tag{A.2}$$

$$\begin{aligned} \alpha_2 = -\frac{1}{6 r_c^2 f_0} \Big[& \alpha_1 (6 r_c f_0 + r_c^2 f_0 \kappa_{-1}) + \alpha_0 \Big(- 2 r_c^2 f_2 - r_c f_1 + f_0 + 2 r_c f_0 \kappa_{-1} \\ & + r_c^2 (f_0 \kappa_0 + f_1 \kappa_{-1}) - m^2 f_0 \Big) \Big] \end{aligned} \tag{A.3}$$

$$\begin{aligned} \alpha_k = -\frac{1}{k(k+1) r_c^2 f_0} \Bigg[& \sum_{j=0}^{k-1} \Big((2j+1)(j+1) r_c f_{k-j-1} - (j+1)(k-2j) r_c^2 f_{k-j} \Big) \alpha_j \\ & + \sum_{j=0}^{k-2} \Big((j+1)^2 f_{k-j-2} - 2(j+1)(k-j-1) r_c f_{k-j-1} \Big) \alpha_j \\ & + \sum_{j=0}^{k-3} -(k-j-2)(j+1) f_{k-j-2} \alpha_j + \sum_{j=0}^{k-1} \alpha_j r_c^2 \sum_{i=0}^{k-j-1} f_i \kappa_{k-j-i-2} \\ & + \sum_{j=0}^{k-2} \alpha_j \Big(\sum_{i=0}^{k-j-2} 2 r_c f_i \kappa_{k-j-i-3} - m^2 f_{k-j-2} \Big) \\ & + \sum_{j=0}^{k-3} \alpha_j \sum_{i=0}^{k-j-3} f_i \kappa_{k-j-i-4} \Bigg] \qquad \text{if } k \geq 3. \end{aligned} \tag{A.4}$$

$$\sigma_0 = 1 \tag{A.5}$$

$$\sigma_1 = 0 \tag{A.6}$$

$$\begin{aligned}\sigma_2 = -\frac{1}{2r_c^2 f_0}\Big[&\mathcal{C}\big(3r_c f_0\alpha_0 + 3r_c^2 f_0\alpha_1\big)\\ &+ \sigma_0\Big(2r_c f_0\kappa_{-1} + r_c^2(f_0\kappa_0 + f_1\kappa_{-1}) - m^2 f_0\Big)\Big]\end{aligned} \tag{A.7}$$

$$\begin{aligned}\sigma_3 = -\frac{1}{6r_c^2 f_0}\Big[&\mathcal{C}\Big(\alpha_0(-r_c^2 f_2 + r_c f_1 + 2f_0) + \alpha_1(2r_c^2 f_1 + 7r_c f_0) + \alpha_2(5r_c^2 f_0)\Big)\\ &+ \sigma_2(6r_c f_0 + r_c^2 f_0\kappa_{-1}) + \sigma_0\Big(f_0\kappa_{-1} + 2r_c(f_0\kappa_0 + f_1\kappa_{-1})\\ &+ r_c^2(f_0\kappa_1 + f_1\kappa_0 + f_2\kappa_{-1}) - m^2 f_1\Big)\Big]\end{aligned} \tag{A.8}$$

$$\begin{aligned}\sigma_k = -\frac{1}{k(k-1)r_c^2 f_0}\Bigg[&(2k-1)r_c^2 f_0\alpha_{k-1}\mathcal{C}\\ &+ \sum_{j=0}^{k-2}\Big((3j-k+2)r_c^2 f_{k-j-1} + (4j+3)r_c f_{k-j-2}\Big)\mathcal{C}\alpha_j\\ &\quad + \Big((j+1)(2j-k+1)r_c^2 f_{k-j-1} + (j+1)(2j+1)r_c f_{k-j-2}\Big)\sigma_{j+1}\\ &+ \sum_{j=0}^{k-3}\Big((2j+2)f_{k-j-3} - 2(k-j-2)r_c f_{k-j-2}\Big)\mathcal{C}\alpha_j\\ &\quad + \Big((j+1)^2 f_{k-j-3} - 2(j+1)(k-j-2)r_c f_{k-j-2}\Big)\sigma_{j+1}\\ &+ \sum_{j=0}^{k-4}\Big(\mathcal{C}\alpha_j + (j+1)\sigma_{j+1}\Big)\Big(-(k-j-3)f_{k-j-3}\Big)\\ &+ \sum_{j=0}^{k-1}\sigma_j\sum_{i=0}^{k-j-1} r_c^2 f_i\kappa_{k-j-i-2} + \sum_{j=0}^{k-2}\sigma_j\Big(2r_c\sum_{i=0}^{k-j-2} f_i\kappa_{k-j-i-3} - m^2 f_{k-j-2}\Big)\\ &+ \sum_{j=0}^{k-3}\sigma_j\sum_{i=0}^{k-j-3} f_i\kappa_{k-j-i-4}\Bigg] \qquad \text{if } k \geq 4.\end{aligned} \tag{A.9}$$

Department of Mathematics
Celestijnenlaan 200B
3001 LEUVEN, BELGIË
tel. + 32 16 32 70 06
fax + 32 16 32 79 98
www.kuleuven.be